The Astrophysical Journal, 972:178 (22pp), 2024 September 10 https://doi.org/10.3847/1538-4357/ad5b56

Exploration of a Dissolving Association Made Up of IC 2602, Tucana–Horologium, and Other Young Comoving Groups

Mark Popinchalk[1,2,3], Jacqueline K. Faherty[1,2], Jonathan Gagné[4,5], Jason L. Curtis[6], Leslie Moranta[4,5], Rocio Kiman[7], Dominic Couture[4,5,8], Alyana Jusino[1], Gaurav Paliwal[1], Ioannis Mouzakitis[1], Nazifa Lamisa[1], Marvin Calderon[1], Izzy Tangney[1], and Jonathan Lacossade[1]

[1] Department of Astrophysics, American Museum of Natural History, Central Park West at 79th Street, New York, NY 10034, USA; popinchalkmark@gmail.com
[2] Physics, The Graduate Center, City University of New York, New York, NY 10016, USA
[3] Department of Physics and Astronomy, Hunter College, City University of New York, 695 Park Avenue, New York, NY 10065, USA
[4] Planétarium Rio Tinto Alcan, Espace pour la Vie, 4801 av. Pierre-de Coubertin, Montréal, Québec, Canada
[5] Trottier Institute for Research on Exoplanets, Université de Montréal, Département de Physique, C.P. 6128 Succ. Centre-ville, Montréal, QC H3C 3J7, Canada
[6] Department of Astronomy, Columbia University, 550 West 120th Street, New York, NY, USA
[7] Department of Astronomy, California Institute of Technology, Pasadena, CA 91125, USA
[8] Département de Physique, Université de Montréal, C.P. 6128 Succ. Centre-ville, Montréal, QC H3C 3J7, Canada
Received 2023 October 3; revised 2024 May 29; accepted 2024 May 31; published 2024 September 5

Abstract

Recently Gagné et al. suggested that young moving groups with similar kinematic properties could be part of larger dissolving structures. One example was IC 2602 as the core of a group of associations, including its corona (CIC 2602), Tucana-Horologium (THA), and parts of Theia 92. We explore this hypothesis by measuring the rotation periods of 953 objects selected using Gaia DR3 kinematics from IC 2602, CIC 2602, Theia 92, and a newly identified group of stars that bridge IC 2602 and THA. We use Transiting Exoplanet Survey Satellite (TESS) full frame images to measure new rotation periods and combine these with the rotation periods for THA from Popinchalk et al. to compare their rotation period distributions and other youth indicators where available to examine if the groups could be coeval. We find strong agreement between the rotation distributions of IC 2602, CIC 2602, and THA, suggesting a shared age of ∼40 Myr, and which in combination could serve as an example of a typical distribution at this age. Theia 92 does not agree at the same level, and we explore the potential kinematic reasons it does not match the rotation period distribution of the larger groups. Additionally, in our light curve analysis we identify ∼50 potential binaries, as well as four new M dwarf complex rotators that show major morphological changes between TESS cycles. Finally, using the amplitudes of the rotation periods we measured, we find strong agreement with the amplitude–age relation presented in Morris for our 40 Myr groups.

Unified Astronomy Thesaurus concepts: Stellar rotation (1629); Moving clusters (1076); Star clusters (1567); Stellar astronomy (1583); Young star clusters (1833); Light curves (918)

Materials only available in the online version of record: figure sets, machine-readable tables

1. Introduction

Stars are similar to humans in that they cannot choose their family. Most stars form in stellar nurseries, coalescing from a large molecular gas cloud. The relative motion of the gas cloud to the galaxy can be inherited by the generation of stars in the form of a shared position or shared UVW velocity (Eggen et al. 1973; de Zeeuw et al. 1999; Zuckerman & Song 2004). Therefore clusters and associations represent outcomes of the star formation process, serving as laboratories of coevolving stars.

These associations exist within our dynamic and complicated galactic environment. The European Space Agency's Gaia Mission (Gaia Collaboration et al. 2016) has revolutionized our ability to identify clusters and associations, allowing for galactic archeology, which provides kinematic evidence of dramatic gravitationally driven sculpting events in certain groups. There is evidence of the galactic potential disrupting associations such as the Hyades, creating tidal tails (Röser et al. 2019). Gagné et al. (2021) suggested that identifying disparate associations that share similar ages and proper motions might be evidence of a larger dissolving moving group.

Gyrochronology is the study of how the rotation period distribution of a population of stars across color–period space changes with time (Barnes 2003). Studies of benchmark clusters such as the Pleiades (Rebull et al. 2016) and Praesepe and Hyades (e.g., Douglas et al. 2017, 2019; Rampalli et al. 2021) have created mile-markers along the road of stellar angular momentum evolution across the spectral type range at 120 Myr and ∼700 Myr, respectively, and other older groups carry that evolution through to billions of years (e.g., Meibom et al. 2011, 2015; Barnes et al. 2016; Gonzalez 2016; Agüeros et al. 2018; Curtis et al. 2019, 2020; Dungee et al. 2022; Gruner et al. 2023).

At ages of 100 Myr and older a "slow-rotator sequence" is clearly defined. Stars of the same mass rotate at approximately the same period, forming a tight sequence across mass with only a small spread in rotation period as they continue to spin down in a Skumanich-like way (i.e., $P_{\rm rot} \propto t^n$ with $n \approx 0.5$; Skumanich 1972). The sequence is developed first in the higher mass stars, with F- and G-type stars at ∼100 Myr as seen in the Pleiades, and then K type by ∼700 Myr as seen in Praesepe and the Hyades, and possibly into the M dwarf regime by a few billion years according to new data for the 4-Gyr-old

cluster M67 (Dungee et al. 2022). It has also been shown to trace velocity dispersion in field stars (Angus et al. 2022).

At ages < 100 Myr, the slow-rotator sequence is not defined. Associations younger than 10 Myr such as Upper Scorpius (Rebull et al. 2018) seem to be dominated by some initial random angular momentum distribution across spectral type, ranging from sub-day to ∼10 days. Popinchalk et al. (2023) noted the potential beginning of the slow-rotator sequence in colors associated with F-type stars in the ∼40 Myr Tucana–Horologium association (THA). Meanwhile, the M dwarfs spin up when comparing groups across the first 50 Myr, which can be interpreted as the stars contracting as they approach the zero-age main sequence (ZAMS; Popinchalk et al. 2021, 2023).

These benchmark clusters and age-dependent features form the core of gyrochronology (Barnes 2003). It has provided a means to confirm the age of young groups (e.g., Gagné et al. 2020; Popinchalk et al. 2023). For example, Curtis et al. (2019) showed the Pisces–Eridanus stream (Meingast et al. 2019) to be far younger than originally suspected, at just ∼120 Myr compared to the original estimate of 1000 Myr. The distribution of rotation periods across color serves as a useful tool for understanding the ages of populations of stars. While individual stars will always carry some unique angular momentum history, considering the distribution of rotation periods across color in a population reveals information about its coevolution.

Rotation periods are not the only result to be drawn from stellar light curves. The shape of the phase-folded light curve has been shown to carry information about the type of variable (Barlow et al. 2022), while Basri & Nguyen (2018) found a relation between the time a light curve displays "double dips" and stellar temperature. This is also important for young stellar populations, with Rebull et al. (2016) and Rebull et al. (2018) showing that there is a diversity of light-curve morphologies, including beat binaries, and dippers. Furthermore, complex rotators (Stauffer et al. 2017; Günther et al. 2022; Popinchalk et al. 2023) are an emerging class of rapidly rotating M dwarfs that have yet to be fully explained.

Additionally, Morris (2020) showed that by defining a "smoothed amplitude" for the light curves of F-, G-, and K-type stars in clusters aged 10 Myr to 4 Gyr, there was a distinct decrease in the mean smoothed amplitude of groups with age. This smoothed amplitude can be interpreted as a proxy for the asymmetric filling fraction of starspots on the surface of the star. This trend is consistent with studies that found that magnetic activity decreases with age (e.g., Mamajek & Hillenbrand 2008; West et al. 2015; Kiman et al. 2021) as starspot size number is thought to be linked to stellar magnetic field strength (e.g., Cao & Pinsonneault 2022).

Other tools exist to describe the youth of objects. X-ray luminosity is an excellent indicator of youth in young associations (Malo et al. 2014; Shkolnik & Barman 2014; Núñez et al. 2022), as young active stars have hotter coronae. Also, the presence of lithium (Li) absorption line at 6707.8 Å is also sensitive to age. Li is depleted in lower layers of stars during their main-sequence lifetimes, but its loss rate is dependent on stellar mass (D'Antona & Mazzitelli 1994). The mass beyond which all Li has been depleted (Li depletion boundary) has been used to age-date young clusters and associations (e.g., Stauffer et al. 1998; Dobbie et al. 2010; Wood et al. 2023).

Moving groups cover vast areas of the sky, and therefore, they can be more challenging to follow up using traditional pointed observations. With all-sky missions such as Gaia Gaia Collaboration et al. (2016) and its latest DR3 release Gaia Collaboration et al. (2023) providing precise photometry and astrometry, along with the Transiting Exoplanet Survey Satellite (TESS; Ricker et al. 2015) providing time series imaging across most of the sky, now is the time to investigate moving groups as components of larger associations.

In this work, we will use rotation period distributions and other semi-independent age-sensitive characteristics to comment on the kinematically derived members of four groups that were identified in Gagné et al. (2021) to potentially be part of a larger dissolving structure. Namely, we will investigate the relationship between IC 2602, the corona of IC 2602 (CIC 2602), THA, Theia 92, and a small population of new stars bridging IC 2602 and THA. By analyzing the similarity of the distributions of age-sensitive measurements for members of each group, we aim to probe the likelihood that they are dissolving components of a previously larger group.

In Section 2, we describe the members of the groups and available data, including their coverage by TESS. In Section 3, we describe our efforts to measure rotation periods for our targets from TESS light curves. We then describe the distributions of several parameters for the groups: in Section 4, we describe their rotation period distributions, in Section 5, we present other available age-sensitive indicators, and in Section 6, we review the photometric amplitudes of the Sun-like stars in each group. We analyze all gyrochronology, age, and kinematic information in Section 7 and summarize conclusions in Section 8.

2. Sample

Gaia's astrometric precision enables the identification of dispersed young moving groups through analysis of their kinematics (e.g., Gagné et al. 2018a; Kounkel & Covey 2019). This has led to catalogs of groups identified by their overdensity in various parameter spaces.

Within this section, we present membership lists for IC 2602, CIC 2602, Theia 92, and one new cohesive population discovered using Gaia DR3 kinematics (Gaia Collaboration et al. 2023) that bridges IC 2602 and THA. For THA we use the membership, rotation periods, and supporting material from Popinchalk et al. (2023), and discuss its kinematic connection to the other groups below. All memberships reported were evaluated using the most recent version of the BANYAN Σ code (Gagné et al. 2018a, described further in 2.2). In this section, we provide a brief overview of the groups and then tabulate individual objects and their observed quantities. We use the Montreal Open Clusters and Associations database (MOCAdb; Gagné et al. in prep) to generate all membership lists. Table 1 lists each source analyzed in this paper with membership classification with the best association, Gaia photometry, kinematic information, the equivalent width (EW) of the Li feature, and X-ray fluxes where available (see Section 2.1).

2.1. Indicators of Youth

Kraus et al. (2014) extensively surveyed THA, and produced Hα and Li measurements of a few hundred members from high-resolution spectra. The other groups in our sample have

Table 1
Membership List

MOCA ID	MOCA Class	DR3 Source ID	Gaia G (mag)	Gaia G_{RP} (mag)	Gaia G_{BP} (mag)	R.A. (deg)	Decl. (deg)	Plx (mas)	RUWE DR3	RV (kms^{-1})	U (kms^{-1})	EWLi (mÅ)	X-Ray Flux ($ergs^{-1}$)
CIC 2602	HM	5239823134370969088	4.69837	4.81876	4.62890	160.558	−64.466	6.75164	0.840257	23.2600	−6.225	⋯	⋯
CIC 2602	CM	5239656077327422336	6.40035	6.38764	6.37737	161.972	−64.262	7.51265	8.571190	⋯	⋯	⋯	⋯
CIC 2602	CM	5237279792173016832	11.60404	10.96990	12.07749	174.249	−65.271	6.46675	0.863967	14.9538	−8.015	⋯	4.820662e-13
CIC 2602	CM	5332922112460126976	11.69818	11.07255	12.15543	177.960	−64.124	6.68291	0.702367	14.8396	−8.172	340.0	⋯
CIC 2602	CM	5332514197981975808	10.99853	10.44968	11.38565	178.089	−64.741	6.85748	0.766239	15.0644	−8.180	⋯	⋯
CIC 2602	HM	5850443307764629376	10.66196	10.07432	11.01196	208.530	−67.562	7.41992	0.909856	12.4796	−6.832	220.0	⋯
CIC 2602	HM	5305964428135613696	15.36091	14.15518	16.89219	146.335	−57.802	6.19233	1.017820	⋯	⋯	⋯	⋯
CIC 2602	CM	5356728158433450880	15.27935	14.04665	16.78195	154.006	−52.355	6.54086	1.028710	⋯	⋯	⋯	⋯
CIC 2602	CM	5356728158433450624	15.31652	14.07066	16.84997	154.007	−52.355	6.59192	1.078790	⋯	⋯	⋯	⋯
CIC 2602	HM	5257760150420250624	15.77533	14.53038	17.39523	145.968	−59.056	6.59784	1.226420	⋯	⋯	⋯	⋯

Note. The membership list of our sample for IC 2602, CIC 2602, Theia 92, and the THA–IC 2602 bridge group. Columns are as follows: MOCA ID, the group name identifier used in MOCAdb; MOCA Class from the BANYAN Σ algorithm (probabilities included in full version); Gaia DR3 Source ID; various values from Gaia DR3 including G, G_{RP}, and G_{BP} magnitudes, R.A., decl., parallax, RUWE, RV; calculated Galactic U velocities from MOCAdb (X, Y, Z, V, and W are available in the full version), Li EWs (references to their publication in the full version), and X-ray fluxes. Uncertainties are also available in the full version. This represents the first 10 rows of our full 953 object list.

(This table is available in its entirety in machine-readable form in the online article.)

not been surveyed to the same extent with dedicated ground-based observing.

However, MOCAdb gathers literature on all-sky measurements useful for age-dating these groups. As such, a limited number of objects in each group were found to have Li EW measurements or X-ray fluxes from ROSAT (Boller et al. 2016). We incorporate those data into Table 1 where available.

2.2. Membership Labels for Each Group

The membership probability for each object was established using the BANYAN Σ Bayesian algorithm that uses multivariate Gaussians in six-dimensional XYZUVW space (Gagné private communication; for algorithm details, see Gagné et al. 2018a). As a secondary criterion, any observational signature of youth was also used to establish the membership category for a given source (e.g., X-ray luminosity, Li abundance, chromospheric emission). Objects were grouped into broad categories that include bona fide (BF), high likelihood (HM), candidate members (CM), low likelihood (LM), and rejected members. BF objects are often founding members of the association that were carefully vetted and have Galactic Cartesian position and velocity (XYZ/UVW) values that define their extent, and also show a clear sign of youth (e.g., X-ray emission, color–magnitude diagram position). HM stars have high BANYAN Σ membership probabilities (>90%), and also have signs of youth. An object might be labeled as HM instead of BF if they are missing either a radial velocity (RV) or a clear sign of youth, even if all other values are a good match to the association's values. CM objects are those that are missing additional measurements (e.g., RV and youth indicator), or whose probability of membership is <90%. LM are objects which have some probability of membership but which is mostly considered negligible, and rejected members are those that were once thought to be part of the group but subsequently were ruled out. For our membership lists we used only sources that fell in the BF, HM, or CM category.

2.2.1. IC 2602

The IC 2602 association is considered the core of the groups analyzed in this paper as outlined by Gagné et al. (2021). The age and motion of IC 2602 have been studied for over 70 yr (Markarian 1953). It's members have been analyzed with Hipparcos (Hoogerwerf & Aguilar 1999; van Leeuwen 1999), and more recently with Gaia (Nisak et al. 2022). Prior to its membership increasing dramatically with Gaia, some of its members were also studied for lithium abundances (Randich et al. 2001a) and rotation periods (Barnes et al. 1999), totaling approximately 30 objects.

The membership list used for this work was derived from the young association database MOCAdb (Gagné et al. in preparation), which examined all previous members and then expanded by using BANYAN Σ on Gaia DR3 data (see Gagné et al. in prep for details). In all, there are 173 members with 109 classified as HM, and 64 as CM.

2.2.2. THA

THA is characterized as part of a loose structure emerging from IC 2602 in Gagné et al. (2021). The core members of THA were first identified by Torres et al. (2000) and Zuckerman & Webb (2000), then combined into one association by Zuckerman et al. (2001). Kraus et al. (2014) conducted a census of the group, including hundreds of spectra from which chromospheric Hα emission and Li EW measurements were derived.

The full membership list of THA used in this work was drawn from Popinchalk et al. (2023), which extended previous lists using Gaia kinematics and BANYAN Σ. In all, there are 368 members with 11 classified as BF, 187 as HM, and 170 as CM.

2.2.3. CIC 2602

The corona of IC 2602, referred herein as CIC 2602, was discovered in Meingast et al. (2021), by using a clustering algorithm that allowed for extended members outside the core of IC 2602 to be identified. This corona is thought to be gravitationally unbound from the core, and likely more affected by the gravitational potential of the Milky Way rather than the core members. Gagné et al. (2021) identified the corona as part of a larger kinematic structure tied to IC 2602 and linked to THA and part of Theia 92. The membership list for CIC 2602 was derived from MOCAdb. In all, there are 259 members with 162 classified as HM, and 97 as CM.

2.2.4. Theia 92

The Theia 92 group was first identified by Kounkel & Covey (2019) and discussed as a dissolving component of the IC 2602 structure in Gagné et al. (2021). As discussed in Gagné et al. (2021), Theia 92 does not appear to be a singular association but rather two stellar populations. Part of Theia 92 appears to be associated with the IC 2602 structure, while another part looks more kinematically consistent with the Platais 8 structure (containing Carina, Columba, Theia 113, and Theia 208). Within this paper we examine each Theia 92 member and we discuss the potential kinematic split in Section 2.4.

The membership list for Theia 92 was derived from MOCAdb (Gagné et al. in prep), which was compiled with the list of all properties from Kounkel & Covey (2019). The defining members were categorized as HM because they have not yet been investigated for signs of youth, although they appear roughly coeval as a whole on a color–magnitude diagram. and then expanded by using BANYAN Σ on Gaia DR3 data (see Gagné et al. in preparation for details). In all, there are 508 members with 129 classified as HM and 379 as CM.

2.2.5. Overlap between Groups

BANYAN Σ creates a probability for each object to be part of a given group, and some objects pass the threshold to be potential members of multiple groups. When this was the case, we placed objects preferentially in IC 2602, then CIC 2602, and then Theia 92. We did this because the populations at the core of IC 2602 are the most robust within BANYAN Σ, followed in turn by CIC 2602. Since Theia 92 was originally defined using a method other than BANYAN Σ, we prioritize the BANYAN Σ results for it after the other two groups.

2.3. New Bridge Objects

As discussed in Gagné et al. (2021), there appears to be a spatial gap between IC 2602 and THA even though they are kinematically coherent. As part of the analysis of the large IC 2602 structure, we searched for stars that might bridge the two

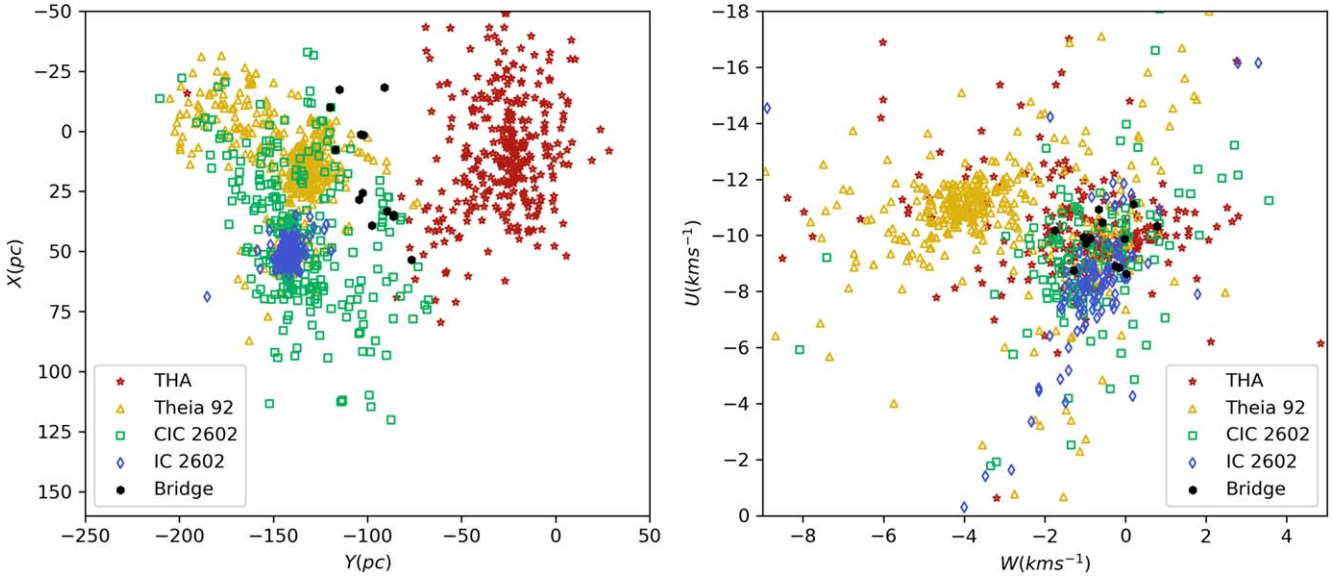

Figure 1. Left: the positions in the X vs. Y plane for our sample. IC 2602 and CIC 2602 are presented as blue diamonds and green squares, respectively. Theia 92 is shown as yellow triangles, THA objects used in Popinchalk et al. (2023) are red stars, and the newly identified bridge group between IC 2602 and THA is shown as black hexagons. Center: U vs. W velocities for our sample. A similar version of this plot was first presented in Gagné et al. (2021).

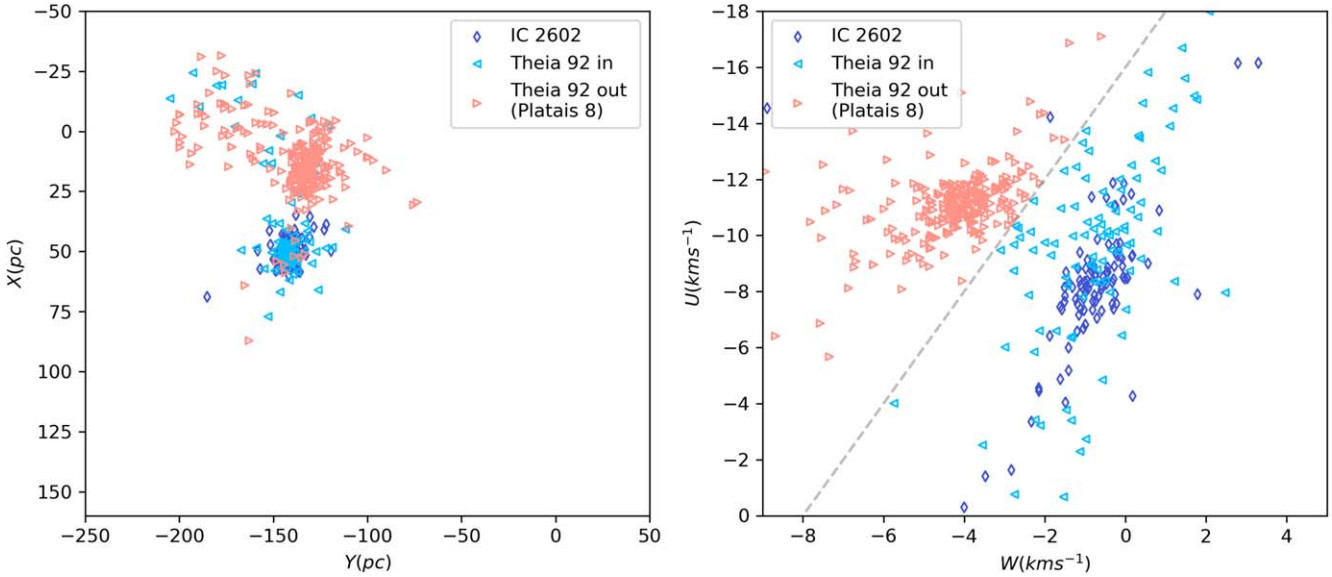

Figure 2. Same as Figure 1 except only showing IC 2602 (blue diamonds) and Theia 92, but the members of Theia 92 have been split into two groups. We define a cut (green-dashed line) through U–W space where one side (light blue left-facing triangles) is similar to the velocity of IC 2602, and the other is not (center-facing coral triangles). Gagné et al. (2021) find that the "out" objects are likely associated with Platais 8. Note that not every object in the sample has UVW velocities.

associations. After analyzing the Gaia DR3 sample, we recovered 13 stars that matched the kinematics of both groups and filled the spatial gap. We have labeled this new group as the "bridge group."

2.4. Distinct Kinematic Populations in Theia 92

All groups discussed in this paper were selected in Gagné et al. (2021) as potential components of a larger dissolving group based on their kinematic similarities. In Figure 1, we recreate a similar description from Gagné et al. (2021) by presenting the overdensity of objects in U–W space.

As discussed above, only part of Theia 92 has similar kinematics to the members of IC 2602, CIC 2602, and THA. Figure 2 shows our division of Theia 92 into two parts as a gray dashed line. We defined a boundary through U–W space where $U = -\frac{16}{8}\,W - 16$. The section labeled "Theia 92 in" is on the side of the line that has a U–W position similar to IC 2602, THA, and CIC 2602, and the other section labeled "Theia 92 out" has a U–W position which is inconsistent. Gagné et al. (2021) note that the "Theia 92 out" objects are likely associated with Platais 8. We chose to analyze the full Theia 92 membership despite much of the group showing divergent U–W values. If the similarity in U–W space does imply a shared history of a dissolving moving group, then the "Theia 92 out" population could show a different gyrochronology relation. We conduct the same analysis on all members of Theia 92 as we do the rest of the sample, but distinguish between the in and out groups of Theia 92 throughout the discussion section below.

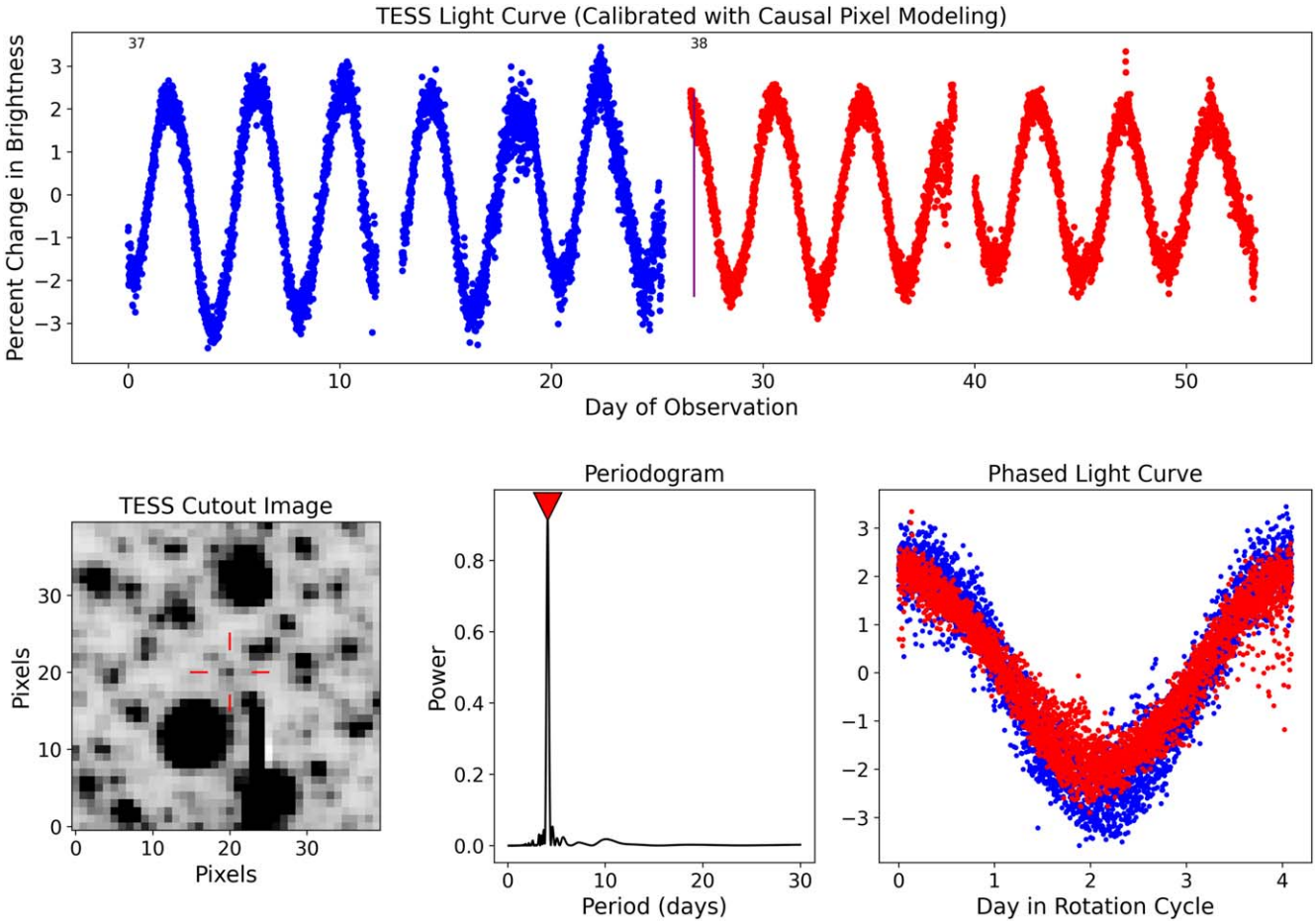

Figure 3. An example four-figured panel for Gaia DR3 5239868587976272896. The top of the figure shows the full light curve of the object, with the two selected sectors being displayed on the plot as red and blue. The purple line in the middle signifies the amplitude from the 5th to 95th percentile across the light curve. At the bottom of the figure from left to center is an image of the TESS FFI cutout (specifically the first cadence of the first sector available), the Lomb–Scargle periodogram, and the phase-folded light curve. During visual inspection we would create multiple panels to determine how to categorize the object. The graph for Gaia DR3 5239868587976272896 demonstrates an example of a "Publish" object as there is a distinct pattern that is present in the full light curve, phased light curve, and a strong peak in the periodogram. Other classifications are described in the text, and the panels that informed the visual inspection for each object are included as a figure set in the online version of this work. (The complete figure set (867 images) is available in the online article.)

3. Rotation Rates from TESS

We used TESS light curves to investigate the groups further. The TESS mission has been extended multiple times, and was in the process of its Cycle 5 observations at the time of this work. This has provided close to all-sky coverage with time series photometry over the course of individual ∼28 day sectors, and often with multiple consecutive sectors of coverage. The cadence of the Full Frame Image (FFI) photometry has increased from 30 minutes in Cycles 1 and 2–10 minutes in Cycles 3 and 4 and again to 2 minutes and 20 s in Cycles 5 and 6. Any of these cadences are more than sufficient for measuring the few hour to multiday rotation periods expected for members of young moving groups.

In this section we describe the process we used to create light curves from TESS FFIs and vet sources for contamination. We also report rotation periods and recovery rates for the objects in our membership lists and comment on objects with light curves of morphological interest.

3.1. Light-curve Creation and Period Classification

We used the same method described in Popinchalk et al. (2023) to create light curves from the FFI of each source. To summarize briefly, from 40 × 40 pixel FFI cutouts downloaded with `TESScut` (Brasseur et al. 2019), we create two light curves using different detrending techniques to remove TESS systematics; one based on a causal pixel model (CPM) from Hattori et al. (2022), and one using simple aperture photometry around the target (SAP).

After observing a variety of light curves across magnitudes, we found that CPM light curves were more suitable for objects with a Gaia $G > 10$ mag, while SAP light curves were more suitable for objects with Gaia $G \leqslant 10$ mag. We cross-checked our choice of light curves as needed during the visual vetting process. Issues such as poor pixels in the CPM method or TESS systematics affecting the SAP method could cause issues with the detrending process. We mitigated this by first visually inspecting all sectors that were available and noting bad sectors before actively selecting remaining sectors and analyzing them in a four-figure panel; as seen in Figure 3.

During this inspection, each panel includes the full light curve of the selected sectors, the Lomb–Scargle periodogram (Lomb 1976; Scargle 1982) for that light curve, a phase-folded light curve based on the peak from the periodogram, and the FFI cutout centered on that object. If needed during the visual inspection, adjustments were made to the range of the percent

Table 2
Rotation Periods Table

DR2 Name	Period (days)	LS Power	Class	Notes	Amplitude (ppm)	Sectors Used	Flares	Flag
5232616282307652352	−1.000000	0.000000	…	…	…	…	…	−1
5232908889837197184	6.928186	0.549534	Good	6.9 in 37 and 7.14 in 11	0.026907	(37)	0	0
5232995132782092672	99.000000	0.040513	Flat	37 bad	0.006694	(10)	0	9
5233078180271139840	0.878836	0.292859	Good	In all, flares 10, 37, 38	0.008858	(10, 11)	1	0
5233112849247719552	3.119741	0.557995	Good	…	0.016602	(63, 64)	0	0
5233136832345571840	2.244071	0.567955	Good	64 bad	0.013991	(10, 11)	1	0
5233181912322787456	2.115008	0.520279	Follow-up	Beat, big gone in 37, dif?	0.015998	(10, 11)	0	2
5233719229910132864	0.987655	0.480355	Good	In all, big flare 38	0.010097	(11)	0	0
5233858833533470720	1.679448	0.116935	Good	11 bad, faint in 37	0.009305	(38)	0	0
5234602653143312256	0.204687	0.437927	Good	In all, second at 0.34	0.012000	(10, 11)	1	0

Note. The rotation periods measured for IC 2602, CIC 2602, Theia 92, and the bridge group. We list the period measured, the power from the Lomb–Scargle periodogram, the Class based on visual inspection to whether the period is acceptable, any notes from the visual inspection, the amplitude of variability, the TESS sectors used to determine the period, and a binary flag for if flares were observed in any part of the light curve, and a final Flag value. A full description of the Class labels and Flag values can be found in the body of the text (Section 3.1).

(This table is available in its entirety in machine-readable form in the online article.)

change in the brightness to avoid possible flares, or to limit the range of period space searched by the periodogram when the maximum peak was influenced by TESS observation windowing rather than an apparent shorter stellar rotation period. We note that these adjustments do not affect the consistency of the analysis, they were only done so that the maximum peak found by the periodogram was the astrophysical signal in the light curve.

From these panels we categorized the objects into four classes: "Publish," "Good," "Flat," or "Garbage." When an object exhibits a strong period in the periodogram and has a distinct periodic pattern in the full and phase-folded light curve, it is classified as "Publish." Objects rated as "Good" have rotation periods that are not as strikingly obvious and distinct as "Publish" objects. We include both "Publish" and "Good" as indicators of successful rotation periods: they represent an esthetic distinction and not a description of certainty, and may prove useful for future work.

Objects with no rotation period present also have panels. These are categorized as "Flat," which are light curves showing no periodicity but appear astrophysical, or "Garbage," meaning objects that only had light curves for sectors with detrending errors or that present non-astrophysical systematics.

In Table 2 we list the rotation periods that were found during this visual inspection. We present the period we measured, the power returned from the Lomb–Scargle periodogram, the category of class we assigned after visual inspection, any notes on the light curve from visual inspection, the amplitude between the 5th and 95th percentile flux values, which sectors were used to measure the period, a column that flags if flares were noted during visual inspection, and the Flag column. The values in the Flag column represent a further classification of the light curves, we list them briefly here but they are explained more thoroughly in their corresponding sections.

1. −1, Not observed in TESS, $N = 86$
2. 0, Good rotation period, $N = 632$
3. 1, Multiple periods in light curve, $N = 25$ (Section 3.3.1)
4. 2, Multiple periods and beat pattern in light curve, $N = 25$ (Section 3.3.1)
5. 3, Aperiodic, $N = 3$
6. 4, Centrifugal breakout and complex rotators, $N = 5$ (Sections 3.3.2 and 3.3.3)
7. 5, Evidence of binary orbits in light curve, $N = 7$ (Section 3.3.1)
8. 6, Removed due to contamination, $N = 53$ (Section 3.2.1)
9. 7, Uncertain, $N = 4$
10. 8, Background eclipsing binary, $N = 2$ (Section 3.3.1)
11. 9, Flat or Garbage, $N = 111$ (Section 3.1)

Note that target objects not observed by TESS are still included in Table 2 and their periods and Flag values are $= -1$ to identify them. These include stars that do not satisfy our blue cut, $(G_{BP} - G_{RP})$ >0.5 mag. This cut was implemented to remove stars bluer than early-F type as their variability is not due to starspot modulation.

3.2. Recovery and Contamination

3.2.1. Contamination

One difficulty in using TESS light curves is that the large pixel size of the telescope can blend light from multiple sources. The 21″ pixels do not provide the same resolution as the Gaia telescope used to identify our targets. Target stars may have their rotation signal diluted due to close neighbors or chance alignments with background stars, even in extended associations such as the groups in this study.

Therefore, contamination depends on our capacity to be certain that the large TESS pixels are clearly describing which source is responsible for the signatures in a light curve. We follow the method detailed in Popinchalk et al. (2023) as a fast set of rules to avoid cases with a high likelihood of contamination. Popinchalk et al. (2023) made two checks for contamination; first inspecting cross-membership contamination, as a straightforward assumption is that young objects in our membership lists are likely to have rotation period signals that may confuse those of the intended target, while field objects are likely quiescent and will not produce spurious signals. Second, another pass is done looking for nearby objects that are of a similar or greater brightness such that they might overwhelm the target's signal. The results of this process are shown in Figure 4 and are discussed fully below.

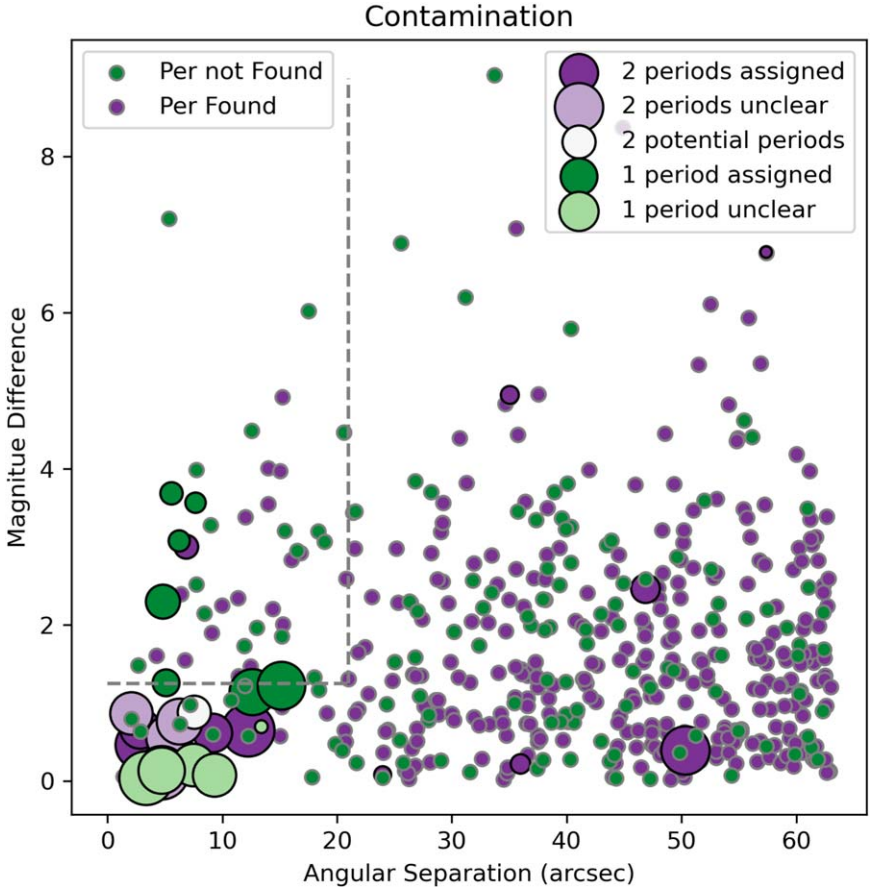

Figure 4. Angular separation (″) vs. the difference in G magnitude for Membership pairs (circles with black edges) and Membership–Gaia pairs (circles with gray points). Membership pairs are color coded based on the status of rotation periods after visually inspecting available light curves for each pair, and presented in the order of the categories described in Section 3.2.1. Purple and white denotes that we found the expected number of periods (two for the case of Membership pairs, one for Membership–Gaia), and green that a rotation period is missing (only one for the case of Membership pairs). The vertical dashed line represents 21″ (≈1 TESS pixel) of separation and the horizontal dashed line is at $\Delta G = 1.25$ mag. We drew these lines based on our Membership pairs, and excluded the 30 objects within them from rotation analysis in case of contamination.

Table 3
Contamination Pairs

Gaia DR2 ID Obj 1	Gaia DR2 ID Obj 2	G 1 (mag)	G 2 (mag)	Δ mag (mag)	Ang. Dist. (arcsec)	P_{rot} 1 (days)	P_{rot} 2 (days)	Score
5217331833720896128	5217331833720894464	14.82374	15.21702	0.39328	50.349019	9.474	1.5955	A
5238048969264890880	5238048969264893696	14.60363	15.15887	0.55524	5.372306	(3.0429)	(1.8939)	B
5238790177556654208	5238790177556654592	14.27162	15.13829	0.86667	2.079402	(2.116)	(5.519)	B
5239293101036428928	5239293101036430720	15.18825	15.84038	0.65213	12.243734	0.8173	0.907	A
5239401432972879872	5239401402934120960	12.60266	15.06769	2.46503	46.865653	5.9626	2.1126	A
5239665320086649472	5239665320086648704	11.30424	14.38108	3.07684	6.240749	5.3389	…	D
5239698855193121664	5239698855172673792	15.78057	15.88919	0.10862	1.050176	(0.277)	…	E
5239736204230183680	5239736204230185344	9.17049	9.86826	0.69777	13.394832	(0.860)	…	E
5239921914293886336	5239921918625122560	15.25637	15.36303	0.10666	4.718489	(1.5709)	(1.4339)	B
5244381331589202048	5244380575683682816	10.34311	10.42604	0.08293	23.975384	2.5590	2.73	A

Note. The pairs of objects within our membership list that we investigated for contamination due to their proximity to one another. Object Gaia DR3 Source IDs, G magnitudes, differences in magnitude, and on-sky angular distance are listed, as well as their flags from visual light-curve inspection. We then assigned a score of A–E (described in the text) to assign their rotation periods, and give our final rotation periods in this table. Uncertain rotation periods are presented in parenthesis (described in the text). Objects with no (…) or uncertain rotation periods had their flag value changed to "6" in the final rotation periods table, representing they were removed due to contamination.

We begin by identifying which stars in the IC 2602, CIC 2602, Theia 92 and bridge group membership lists have a potential nearby contaminant. Across all the groups and all the sources, we find 30 pairs where a given member is within 1′ another member (≈3 TESS pixels). We then examine their individual magnitudes, their difference in magnitude, their separation, and the panels created during visual period identification. We present all this information in Table 3.

We sorted the 30 pairs into six cases:

1. A: Pairs where we had two periods and we could assign a period to each member with confidence.

2. B: Pairs where we had two periods but it was unclear to which star they should be assigned.
3. C: Pairs with one obvious period, and a potential secondary period.
4. D: Pairs with only one period, which we could assign to a specific member with confidence.
5. E: Pairs with only one period and it was unclear to which star it should be assigned.
6. X: No periods detected.

The ABCDEX flags are specifically for sorting the pairs of potential contaminating objects within the sample. They describe how many periods appear in the blended light curves and if we can assign them to a particular object. The numerical Flag column in Table 2 is used to sort the entire sample into final classifications that inform whether we use them in our rotation analysis. Each pair is assigned an ABCDEX flag, while objects within the pair receive a 0–9 Flag value.

We list our categorization for each of the 30 pairs in Table 3. When we could assign the period to a specific star (such as in cases A and D) we list the period. When we could not confidently assign the period (such as in cases B and E) we placed it in parenthesis, and if there were fewer periods than expected (case E) the period column is denoted by an ellipsis for the fainter star.

Below, we enumerate three particularly interesting cases. The light curves for Gaia DR3 5239698855193121664 and Gaia DR3 5239698855172673792 show dips from an eclipsing binary, as well as a rotation period. From our binary analysis (See Section 3.3.1) that inspects a 5×5 grid of pixels centered on the target, we are confident the dips are from the source's pixel. However, we are not sure which, if either, of our objects it is from. Neither object has an unusually high RUWE value. Since we do not know where to assign the rotation period, we give it a case score of E.

The light curves for Gaia DR3 5257590761237066624 and Gaia DR3 5257590761237068288 show no rotation period signal at all. Gaia DR3 5257590761237066624 is Gaia $G \approx 9$, six magnitudes brighter than the other member in the pair, so we would expect to see only one rotation period from the brighter member. However, Gaia DR3 5257590761237066624 has a $(G_{BP} - G_{RP}) = 0.55$, and is listed in SIMBAD as a F2 spectral type. Therefore even though it passed our cut of $(G_{BP} - G_{RP}) > 0.5$, it may be too hot to have starspots on its surface. This was the only case that was categorized as X, and we did not consider it further in our contamination analysis.

Additionally, we note that while we confidently assigned periods to Gaia DR3 5321265300647263232 and Gaia DR3 5321265403726473088, only the latter has a rotation period. Gaia DR3 5321265300647263232 is likely a heartbeat binary, and discussed more in Section 3.3.1.

Finally, objects in our contamination pairs with no or uncertain rotation periods were given a value of "6" in the Flag column of Table 2, indicating that they were removed due to contamination.

We also searched for background field star contamination. Assuming that a generic Gaia star is likely part of the field and quiescent at a few Gyr, they will not show signs of starspot variability. Field stars will only contaminate the starspot variability of a target in our sample if (1) they are close enough to share TESS pixels and (2) they are a similar magnitude or brighter than the target star, as the additional flux will minimize or even dominate the rotation signal. We searched for objects near our sources ($< 63''$ or ≈ 3 TESS pixels) that were brighter in Gaia G than the target, meaning they had a positive ΔG. Popinchalk et al. (2023) found that background sources with angular separations $> 42''$ or two TESS pixels and $\Delta G > 2$ could contaminate the target light curve. More conservatively, Boyle & Bouma (2023) set their limit of contamination at one TESS pixel and one-tenth brighter. We based our cutoff on the analysis conducted with the young star pairs, noting that we were still mostly able to assign periods for pairs within $21''$ for that sample. In all, we found 30 of the young objects with a Gaia source brighter than $\Delta G = 1.25$ and within $21''$. We flagged all 30 objects with a Flag value = "6" in Table 2, representing that they have been removed due to contamination, and not considered them in further rotation period analysis.

3.2.2. Recovery

The recovery rate of the stellar rotation period for a population of stars is influenced by both observational and astrophysical effects. Observationally, sources may be too faint for the telescope. Astrophysically, sources might be oriented pole-on (or close to pole-on) limiting the photometric variability due to rotation as starspots fail to move in and out of view. Furthermore, the intrinsic variability of the star can be so low that it is beyond the detectability of the telescope.

Our total recovery rate across the full membership sample was 80% (e.g., 78% for IC 2602, 81% for Theia 92). We present an example histogram of the recovery rate of IC 2602 in Figure 5 in the cross section of Gaia G mag and $(G - G_{RP})$ color.

All three newly analyzed groups—IC 2602, CIC 2602, and Theia 92—show similar features in their histograms. In the upper Gaia G panels, the recovery rate tends to be lower in the final two bins nearest the Gaia $G = 16$ cutoff. This is expected as stellar variability in fainter stars will be rivaled by telescope systematics and photometric noise and so will be harder to detect. There is no clear trend in recovery rate for the lower Gaia $(G - G_{RP})$ panels, although IC 2602 does show unusually low recovery rates at Gaia $(G - G_{RP}) = 1.2$–1.3.

We note that there is a dearth of G and K stars at Gaia $(G - G_{RP}) = 0.65$–0.8 in both IC 2602 and CIC 2602. There is no obvious astrophysical reason why there should be a lack of these stars due to an initial mass function argument (Luhman 2022, 2023). Instead, this is observed in all young associations, and is a reflection that effective temperature is extremely sensitive to mass in this range of masses at young ages. We draw attention to it only as it impacts our analysis in further sections.

3.3. Interesting Light Curves

3.3.1. Multiple Periods and Candidate Binaries

We present color–magnitude diagrams (CMDs) for each young group in Figure 6. The full membership list is shown with gray points, while those that have some indication of binarity have been overplotted as follows.

In purple, we denote objects with a Gaia DR3 re-normalized unit weight error for the astrometric solution (RUWE) greater than 1.4. The single-star astrometric solution (Lindegren et al. 2012, 2021) is the assumed model for Gaia sources, so if the object's position time series deviates from the expected value of 1, it could be due to an unresolved companion (e.g., Belokurov et al. 2020; Stassun & Torres 2021). While Palumbo et al. (2022) noted a color dependence in THA with RUWE in

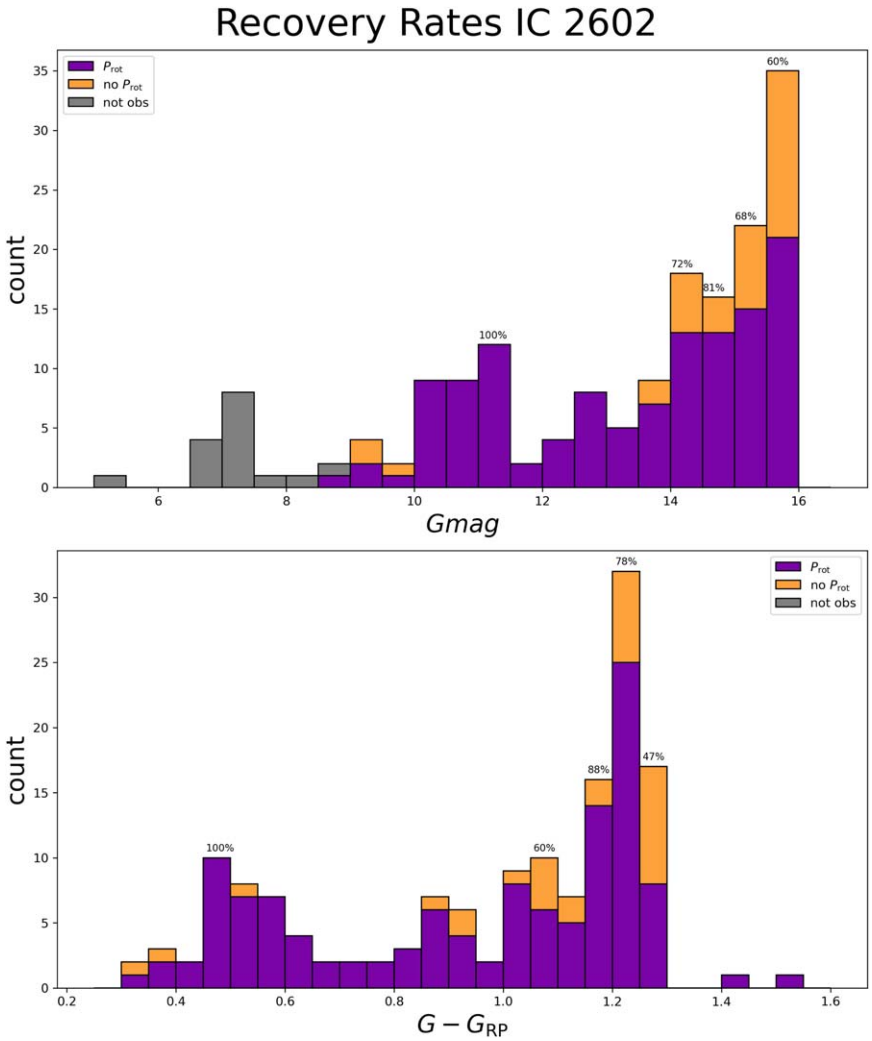

Figure 5. The histogram representing the recovery of rotation period signals in IC 2602. The top panel shows the recovery rate across Gaia G , and the bottom panel for Gaia ($G - G_{RP}$). The gray shaded areas represent stars that no TESS light curve was downloaded for, either because they were not observed by TESS or they were too blue as we did not consider early-F stars with ($G_{BP} - G_{RP}$) <0.5 mag (see Section 3.1). Purple represents stars for which periodic signals were recovered, including objects with Flag values of 0 (rotation period), 1 (multiple periods), 2 (beat periods), 3 (aperiodic periodicity), 4 (complex rotators) and 5 (eclipsing binaries). The orange shaded region represents stars for which no periodic signal was found including Flag value = 6 (removed due to contamination) and Flag value = 9 (Flat or Garbage from visual inspection). Not all the brightest objects in the top panel are shown in the bottom, as we only include the equivalent Gaia ($G - G_{RP}$) range to represent F–M stars. The same style of Figure for CIC 2602 and Theia 92 are included as a Figure set in the online version.
(The complete figure set (3 images) is available in the online article.)

the M dwarf regime, Mejías et al. (2022) have shown that it is useful for detecting potential binaries for M dwarfs in particular.

Other binary candidates were selected based on the visual light-curve analysis described in Section 3.1. During the process of rotation rate recovery, we noted light curves that exhibited multiple periods with a Flag value of 1. These sources are colored as blue points in Figure 6. Multiple period sources have been interpreted in the literature to be caused by rotation periods from each member of a companion system (e.g., Shan et al. 2017; Stauffer et al. 2018a; Tokovinin & Briceño 2018). For each source, we made sure that the additional period was not an obvious harmonic of the most prominent period, which is a feature of light curves with "double dips" (e.g., Basri & Nguyen 2018). We also ensured that each source had a unique light-curve morphology when phase folded on the additional period.

A subset of these multiple period light curves were those with beat patterns, which we colored with orange points in Figure 6. Each of these sources was given a Flag value of 3 in Table 2. These beat patterns have been used as evidence for binary systems with similar rotation periods (e.g., Paudel et al. 2019), but could also be related to differential rotation of multiple starspots at different latitudes on the stellar surface (e.g., Reinhold et al. 2013). We remain agnostic about the cause of the beat patterns, but discuss possibilities in disentangling them within the data in Section 7.

Finally, during our visual inspection of light curves we noted objects with dips that were consistent with eclipsing binaries. These were given the Flag value of 5, and are presented as green points in Figure 6. To confirm that the dips were originating in our target pixel, we created CPM light curves for a 5×5 grid of pixels centered around our target pixel, an example of which can be seen in Figure 7.

These 25 pixel light curves were then inspected to see where the dips were deepest. If the target pixel had the deepest dips, we attributed them to coming from our source and listed it as an eclipsing binary. If they did not, we assumed it was from a

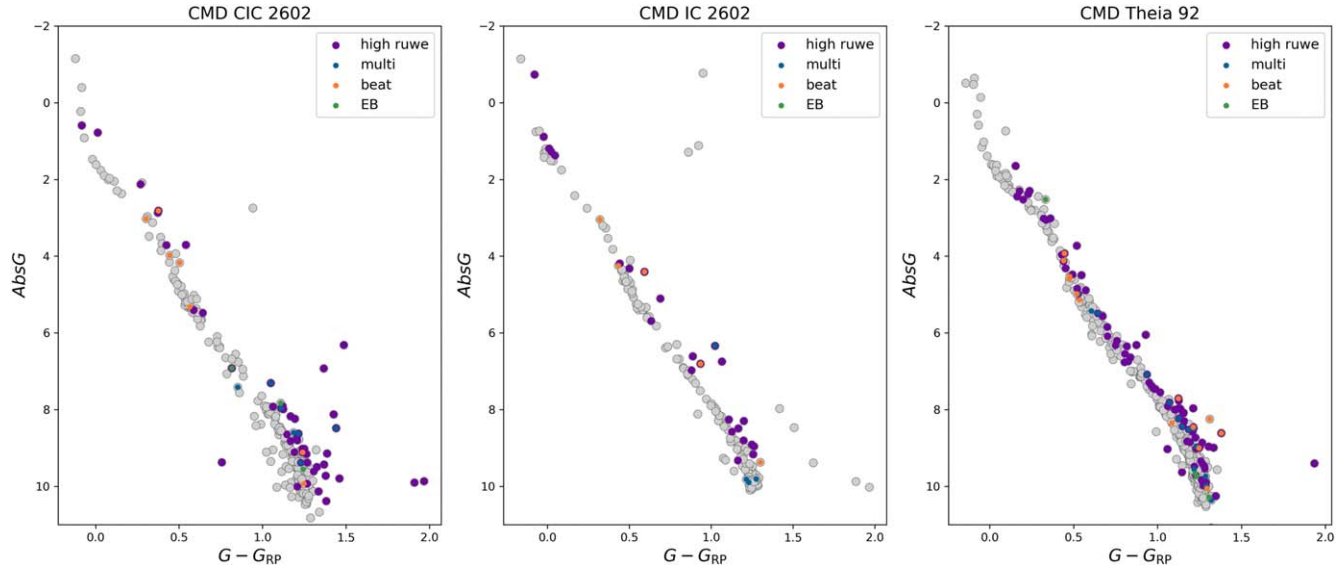

Figure 6. Color–magnitude diagrams of each group in our sample, with absolute magnitude M_G vs. Gaia $(G - G_{RP})$. Objects in the sample are gray points, on which are overlaid a variety of colorful points. Purple points are objects with anomalous Gaia DR3 RUWE values, which can be indicative of a companion. Blue points are objects with multiple periods in their light curves, orange are those that the multiple periods are so similar that a beat pattern appears in the light curve. Finally, green points are objects that show transits consistent with eclipsing binaries, and in one case a heartbeat binary pattern. These colored points tend to trace the more luminous side of the spread of the main sequence, consistent with additional contribution from a companion.

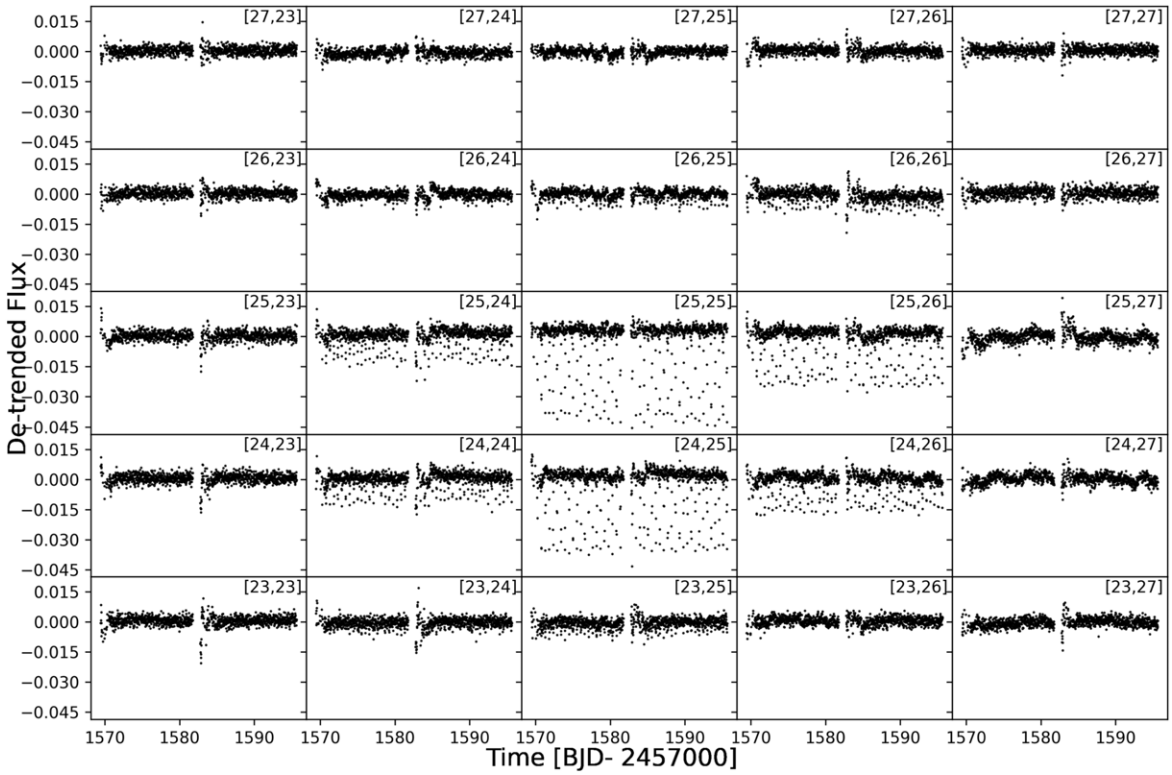

Figure 7. Pixel-specific light curves for the 5 × 5 grid of pixels centered around the target's pixel for Gaia DR3 5240531632175135616, which was flagged for EB-like transits during visual inspection. All pixels were detrended using the CPM method described in 3.1. While the transit dips are present in several of the adjoining pixels, they are deepest in the target pixel and we attribute them to be from our target.

background source. This was the case for Gaia DR3 5238636383359706368 and Gaia DR3 5313715637187632512. They were given a Flag value = 6 as well in the final rotation period table, which removed them from further analysis.

We also included among the eclipsing binaries Gaia DR3 5321265300647263232, also known as HD 73463, whose panel is shown in Figure 8. Heartbeat stars have been identified in TESS (e.g., Kołaczek-Szymański et al. 2021) and are interpreted as a close tidal interaction between binary companions warping the shape of a member into an ellipse and changing the surface area and therefore luminosity. HD 73463 was previously identified as a spectroscopic binary, and had RV measurements that yielded a period of 1.779 ± 0.002 days (Gieseking 1981). This is a discrepant value from our 2.207 day TESS light-curve period, which we

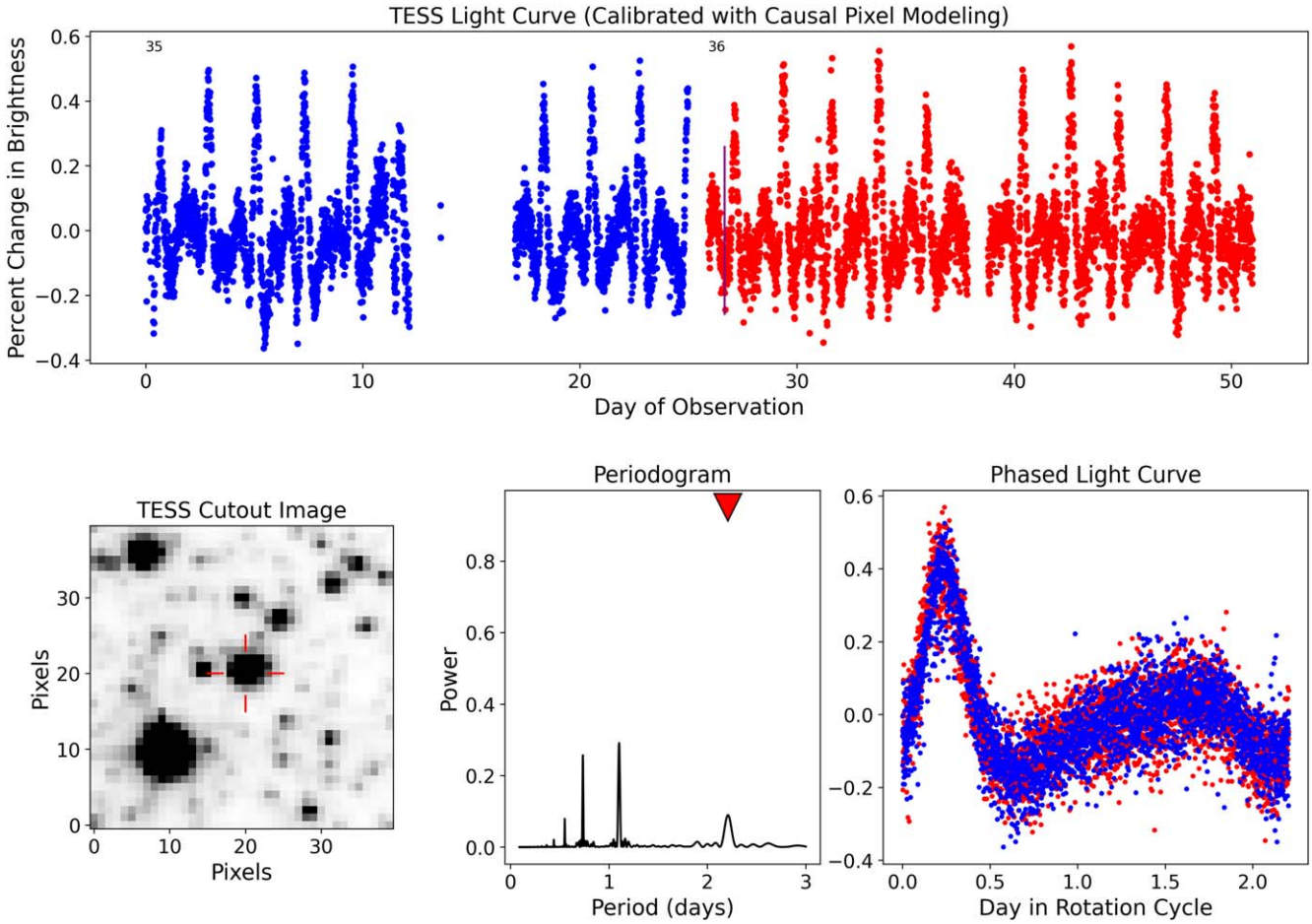

Figure 8. Same as Figure 3, but for Gaia DR3 5321265300647263232, also known as HD 73463. Previously identified as a spectroscopic binary, the light curve shows a heartbeat signature typical of binary systems.

attribute to the number of data points used in the RV period (it is derived from ∼10 observations over the course of 100 days).

The light curve alone is not sufficient to rule out binarity. The objects in these associations are within only a few hundred parsecs, which means that wide binary systems (e.g., Andrews et al. 2017; Deacon & Kraus 2020) can extend for tens of arcseconds to arcminutes. These systems would be resolved in surveys such as Gaia. Therefore, there may be binary systems within this sample that cannot be identified using light curves, as it is possible for companions to be outside of a single TESS pixel from one another. We attempt to account for nearby neighbors in Section 3.2.1.

In summary, we found 25 objects with multiple periods in their light curve (Flag value = 1 in Table 2), 25 with "beat" patterns (Flag value = 2), and seven that showed binary orbit signatures (six with eclipsing transits, and one with a heartbeat pattern, all assigned Flag value = 5).

3.3.2. Centrifugal Breakout Objects

Palumbo et al. (2022) describe TIC 234284556, a THA M dwarf with a light curve featuring a corotating feature with a period consistent with that of the rotation period. The feature is a relatively sharp dip that appears in Sectors 1 and 27, and eventually disappears from the light curve in Sector 27. This was interpreted as most likely being a magnetospheric cloud experiencing centrifugal breakout.

We found a single object that could be considered similar to that described in Palumbo et al. (2022). We created light curves for Sectors 11, 12, and 37–39 for Gaia DR3 5205301321086705408 as part of our light-curve creation process. During visual inspection we noticed a small dip in Sector 38 along with the rotation period, but not present in any of the other sectors. We list it here for potential follow-up work describing these as a class of objects, and assign it the Flag value = 4.

3.3.3. Complex Rotators

Complex rotators were first identified in Stauffer et al. (2017), and additional identification of objects (e.g., Stauffer et al. 2018b; Zhan et al. 2019) has shown that it is a phenomenon for young, rapidly rotating (< 1 day) M dwarfs (the oldest was ∼120 Myr and identified in the Pleiades by Rebull et al. 2016). The rapid and complex modulation in the light-curve morphology has been shown to be very stable on the order of months, but alters over the course of years (see Koen 2023; Popinchalk et al. 2023). The theoretical root cause of the phenomenon is discussed thoroughly in Günther et al. (2022), with a prevailing model being a sight-line-dependent variability due to corotating clouds of material held at a Keplerian orbit consistent with the rotation of the star. Through our visual inspection of the light curves we identified four new complex rotators.

The four new complex rotators within the groups analyzed in this work are displayed in Figure 9. We show the light curves

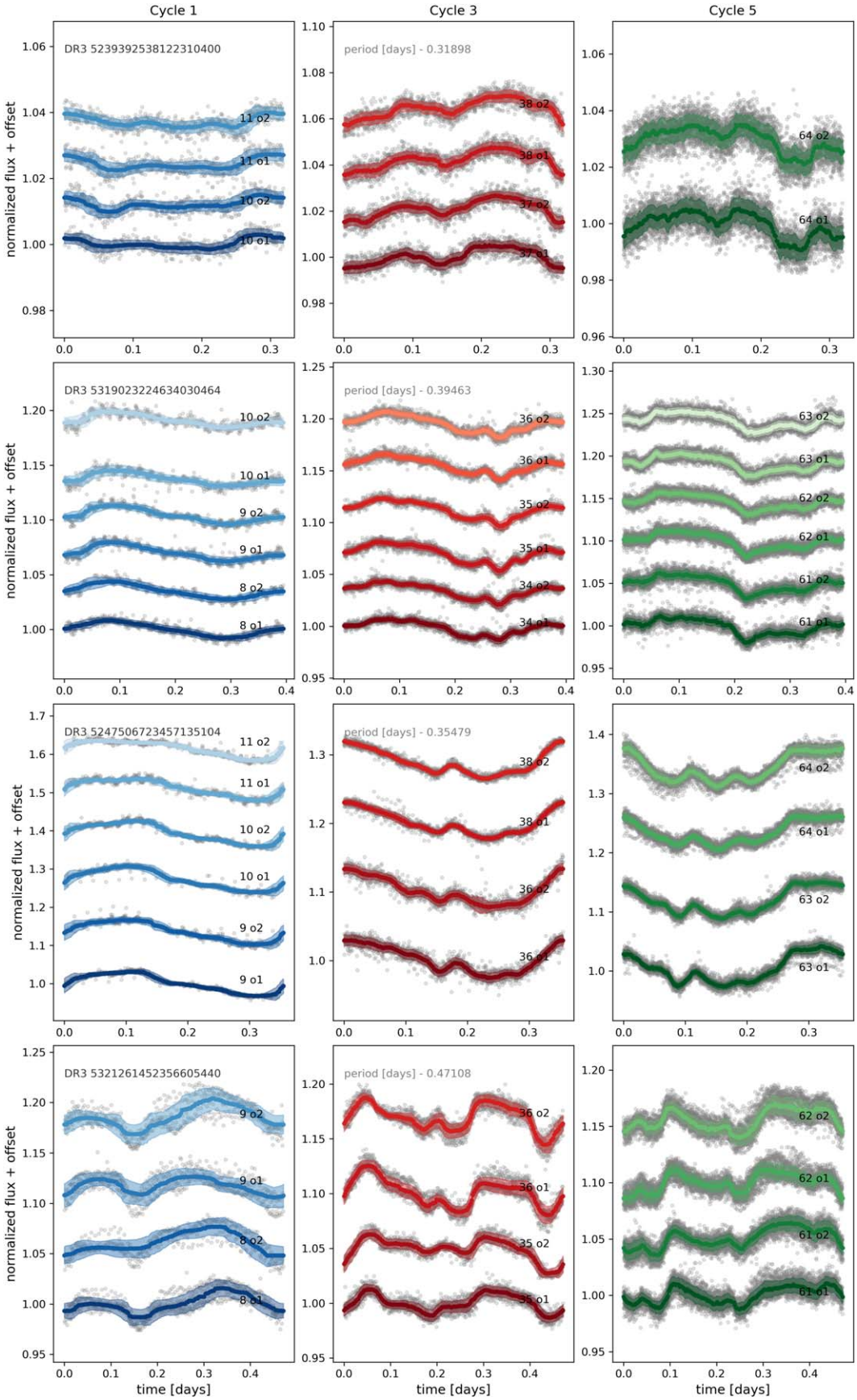

Figure 9. Four new complex rotators identified from objects in this work. Gaia DR3 5239392538122310400 and 5247506723457135104are from IC 2602, while 5319023224634030464 and 5321261452356605440 are in CIC 2602 and Theia 92, respectively. Each column represents a different cycle of TESS observation for each object and is made from the FFIs, moving from Cycle 1 and 30 minute cadence in blue on the left, to Cycle 3 and 10 minute cadence in red, and Cycle 5 with 200 s cadence in green. Each sector is divided into the two orbits of TESS, with earlier observations at the bottom of each panel.

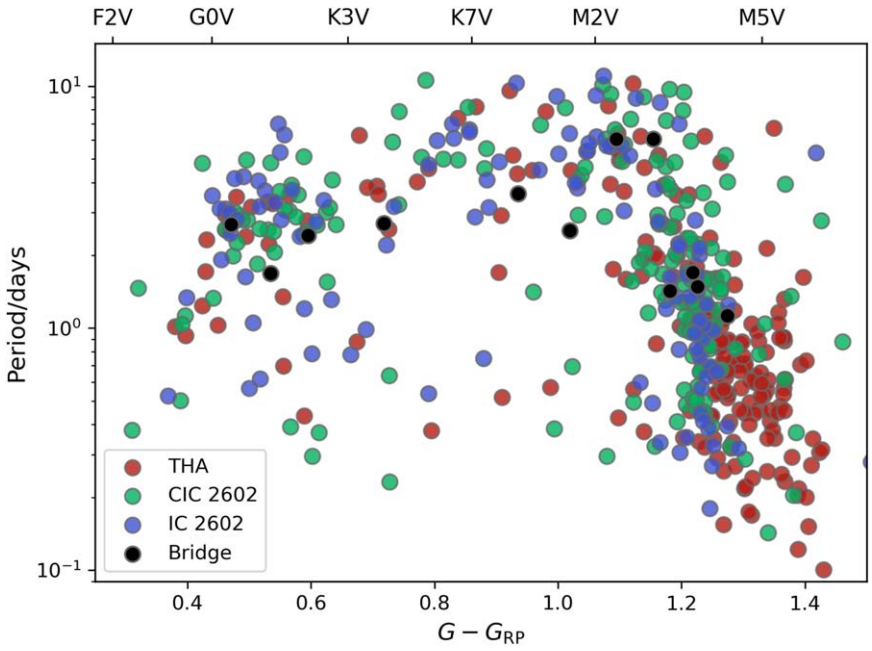

Figure 10. The Gaia ($G - G_{RP}$) color vs. log period distribution of IC 2602 (blue), compared to those of CIC 2602 (green), THA (red), and the bridge group (black). Approximate spectral types run along the top axis.

for each sector. These are the same light curves used for rotation period analysis, derived from the FFIs and detrended using a Causal Pixel Model (see Section 3.1). The different cadence for each cycle (30 minutes, 10 minutes, and 200 s for Cycles 1, 3, and 5, respectively) means there are more data for each sector moving right to left in the plot. Each sector is subdivided into the two orbits of TESS during that sector, to provide a further description of the morphology over shorter (week-long) timescales.

In general, it is easier to see the complexity of the light curves in the middle and right columns representing Cycles 3 and 5, respectively. The shorter cadence in the later cycles seems better suited to capture the detail. Most of the previous complex rotators discovered in TESS were found in 2 minute postage stamps (e.g., Zhan et al. 2019). Günther et al. (2022) showed that for the same observing window, a shorter cadence revealed more detail, although complex rotators were discovered in both K2 and TESS at 30 minute cadence (e.g., Stauffer et al. 2017; Popinchalk et al. 2023). While not surprising, this does show that FFI observations beyond Cycle 3 are at a short enough cadence to capture the fine detail of the morphology, and the 200 s cadence from Cycle 5 onward can likely rival the detail of previous cycles' 2 minute postage stamps.

Comparing the light-curve morphology across time for the objects, we see a gradual change within each cycle, and large differences between disparate cycles (e.g., Cycle 1 versus Cycle 5). Koen (2023) and Popinchalk et al. (2023) both previously noted that morphologies do change between cycles, but there is still more to understand about how often they change. For example, Popinchalk et al. (2023) found a complex rotator that lost all complexity between cycles, a phenomenon that does not show up in our sample. There is less obvious complexity in Cycle 1, likely due to the 30 minute cadence mentioned above.

4. Rotation Period Distributions

In Figures 10, 11, and 12, we present the color–period distribution of all BF, HM, and CM objects from IC 2602, CIC 2602, THA, and Theia 92. We use Gaia ($G - G_{RP}$) for our color x-axis, and the rotation periods in a logarithmic scale for our y-axis. Approximate spectral types run along the top axis.[9] We only include objects with a Flag value of 0, which represent objects with good rotation periods with no contamination or signature of binarity (see Section 3.2). In the following sections we will compare the rotation periods of the various groups to IC 2602, as they should be similar if they are indeed part of a large dissolving structure with IC 2602 as its core.

4.1. IC 2602, CIC 2602, and THA

In Figure 10 we show members of IC 2602, CIC 2602, THA, and the bridge group between IC 2602 and THA. As IC 2602 is thought to be the core of this dissolving structure, we focus on that shape as we compare and contrast the other groups. Overall, we find that the CIC 2602 and THA overlap consistently across the color–period diagram, confirming that they are well matched as coeval groups. Most G to K spectral types have periods $>$ 1 day and increase in rotation period toward a peak at Gaia ($G - G_{RP}$) $\sim$1.1, whereafter stars in the M dwarf are more quickly rotating.

Popinchalk et al. (2023) traced the start of the slow-rotator sequence to the start of G0 class in THA, and we see a similar hint of convergence for Gaia ($G - G_{RP}$) < 0.5. We note that the G-type stars in IC 2602 and CIC 2602 show more scatter than that of THA at the same color (Gaia ($G - G_{RP}$) = 0.5–0.6). They overlap with the THA distribution in this range, but also have several objects that are above THA and spinning more slowly, especially in IC

[9] Based on http://www.pas.rochester.edu/~emamajek/EEM_dwarf_UBVIJHK_colors_Teff.txt (see Pecaut & Mamajek 2013).

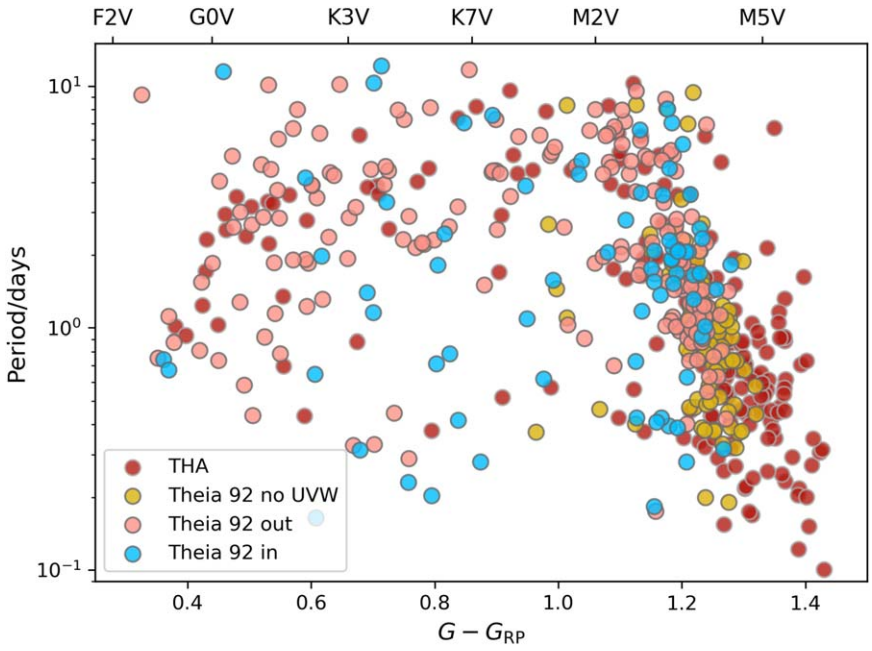

Figure 11. The color–period distribution of Theia 92 split into three subsets; those with UVW velocities consistent with IC 2602 (light blue), inconsistent (coral), and those without UVW velocities (yellow) compared to the rotation period distribution of THA (red). Axes are the same as Figure 10.

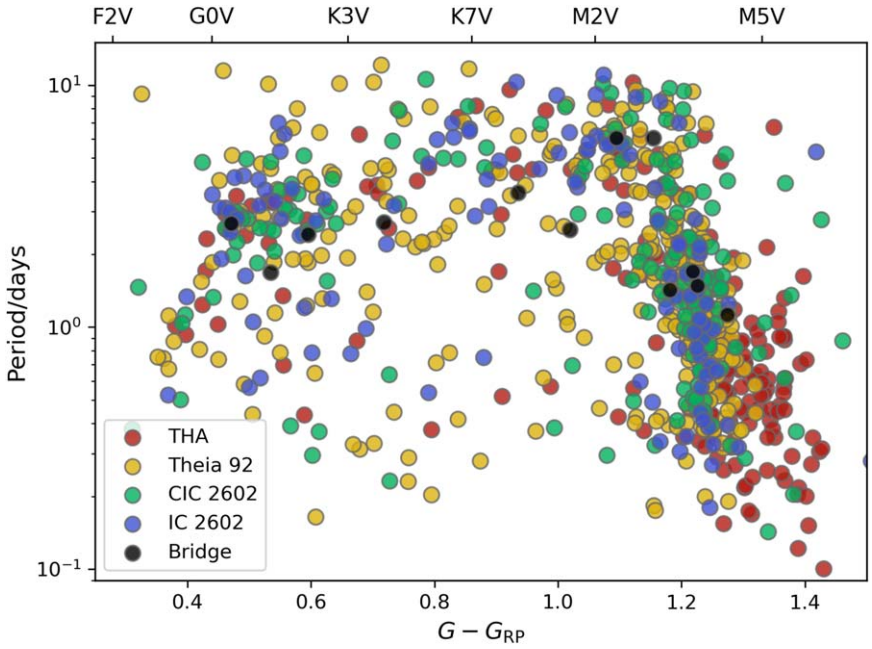

Figure 12. The color–period distribution of the four new groups presented in this work: IC 2602 (blue), CIC 2602 (green), the bridge group (black), and Theia 92 (yellow), with THA (red) from Popinchalk et al. (2023) for comparison. The M dwarf regime is the most consistent across all the groups, showing clearly faster-rotating objects moving redward in color from Gaia ($G - G_{RP}$) ∼1.1. Axes are the same as Figure 10.

2602. This is discussed further in Section 7. It is hard to see if this trend continues into the K-type stars because there is a distinct lack of objects for both IC 2602 and CIC 2602 between Gaia ($G - G_{RP}$) = 0.6–0.8, mentioned in Section 3.2. This makes describing the distribution at these colors challenging, similar to the gap in G stars in the THA distribution mentioned in Popinchalk et al. (2023).

The most similar region between all the groups is the M dwarf regime at Gaia ($G - G_{RP}$) $\gtrsim$ 1.1, where there is a noticeable decrease in rotation period from Gaia ($G - G_{RP}$) = 1.15–1.3. We note that the gray THA distribution reaches rapidly rotating M5 objects at Gaia ($G - G_{RP}$) = 1.4, while the IC 2602 and CIC 2602 samples reach to ∼1.3. We attribute this to a selection bias, as our strict magnitude cutoff at $G = 16$ would rule out more mid-to-late M objects with their intrinsically dimmer luminosities. This is exacerbated as most of IC 2602 and CIC 2602 are close to 100 pc further than THA, which would contribute to the dimmer stars not reaching the magnitude cutoff. There are ∼10 members of CIC 2062 that do extend beyond Gaia ($G - G_{RP}$) = 1.3 and do not fall on top of the THA distribution. Palumbo et al. (2022) point out that Gaia DR2 RUWE is questionable in the red part of the M dwarf

regime in THA, and when expected we found these objects did too. There may be a chance they have spurious Gaia magnitudes as well, and while they do not fall on the main distribution, they are not outside of the full range of THA members at those colors. Regardless, the distribution of the rotation periods for IC 2602 and its potential dissolving components of THA and CIC 2602 all appear very similar.

4.1.1. The IC 2602 to THA bridge

There are only a limited number of objects within the bridge group, but they appear extremely consistent with IC 2602 and its kinematic partners. Examining Figure 10, we see that all the objects in the bridge group with colors Gaia $(G - G_{RP}) < 1$ are not rotating quickly and are consistent with the main distribution of stars for their color in IC 2602, CIC 2602, and THA. Additionally, the M dwarf stars are falling right on top of the M dwarf distributions of the other groups.

4.2. Theia 92

In Figure 11 we present the rotation period distribution of the objects in Theia 92. We use the THA rotations as a comparison. Since we established that THA is similar to IC 2602 and is a factor of two larger in membership it serves as an easy comparison without overcrowding the plots with multiple groups. We divide Theia 92 based on the *UVW* cuts described in Section 2.4, intended to distinguish between the parts of Theia 92 that are more similar to IC 2602 kinematically (light blue) and those that are not (coral). As a reminder, (Gagné et al. 2021) found that the "out" population is kinematically related to Platais 8. *UVW* velocities require 6D kinematics, and those missing any (typically an RV) did not have a value to compare against, and are plotted in yellow; they are mostly M stars.

For objects outside of the *UVW* cut (coral), the structure of the FGK regime distribution seems somewhat similar to THA but with additional scatter. Most are spinning with a period > 1 day, but show a huge scatter in that range, with several objects with period $\geqslant 10$ days. The lack of almost any < 1 day rotation periods could be indicative of a population that has begun to slow down in this regime, which could be consistent with a similar age population to THA, but not as similar as IC 2602 and CIC 2602. In the redder M dwarf regime, objects do follow the THA/IC 2602 M dwarf distribution, from Gaia $(G - G_{RP}) \sim 1.1$ on, but similarly stop around Gaia $(G - G_{RP}) \sim 1.3$, which we again attribute to a magnitude cutoff.

For objects within the *UVW* cut (light blue), it is also challenging to see a similarity with that of THA in the FGK range. This may be due to the small number of objects (< 30), but even these show a wide range of young periods from < 1 day to > 10 days at all colors. However, in the M dwarf regime the distribution falls mostly on that of IC 2602, CIC 2602, and THA.

Finally, the objects without *UVW* velocities are shown in yellow. The vast majority of these are M dwarfs, and they too fall on the matching distribution of THA, IC 2602, and CIC 2602.

4.3. Full Sample Comparison

Figure 12 shows all groups analyzed in this paper—IC 2602, CIC 2602, THA, Theia 92, and the bridge group—in color–period space. All the rotations we measured are < 10 days, meaning the objects displayed are likely young. However, at any color there is a large spread in the Theia 92 sample, somewhat evenly distributed across the FGK spectral type color ranges. This could be evidence of a mix of populations with differing young ages.

In summary, we find that IC 2602, CIC 2602, THA, and the bridge group are well matched as a cohesive association in color–period space. Theia 92 has strong overlap but the scatter in the FGK regime (even with a split in *UVW* space) is challenging to reconcile with the IC 2602 core group.

5. Other Youth Indicators

5.1. Lithium Absorption

In Figure 13, literature values for the EW of the Li I 6708 Å line are plotted against Gaia $(G - G_{RP})$ for each object newly analyzed in this paper. As mentioned in Section 2, these values were compiled by Gagné et al. (in prep) and reported in the MOCAdb. The values come from Randich et al. (1997, 2001b), Torres et al. (2006), and da Silva et al. (2009). Randich et al. (1997, 2001b) explicitly deblend the Fe I 6707.44 Å line while Torres et al. (2006) and da Silva et al. (2009) use synthetic models to estimate the Li abundance. We refer the reader to relevant publications for more details. The THA values were compiled as discussed in Popinchalk et al. (2023). We use the Pleiades cluster as a benchmark comparison, drawing the Li EW values from Bouvier et al. (2018).

There are not enough objects with Li measurements over all the groups to cover the full color range of members. However, those that are available map well to each other with a scatter consistent with a ~40 Myr association.

5.2. Coronal X-Rays

For objects with X-ray fluxes from ROSAT (Boller et al. 2016), we calculate the X-ray luminosity using

$$L_X = 1.20 \times 10^{38} \times f_X \times D^2, \quad (1)$$

where f_X is the X-ray flux drawn from hardness ratio 1 (Boller et al. 2016), and D is the distance calculated from the Gaia DR3 parallax.

In Figure 14 we plot the X-ray luminosities against Gaia $(G - G_{RP})$ for each object with available data, adding ROSAT values for Pleiades objects as black stars for reference. Approximate spectral types run along the upper axis. Just as with the Li EW, we do not have full coverage across spectral type/color for every group. However, even with the small numbers from each individual group, we find that the overall trend is that all associations analyzed are consistent with each other, reaffirming the cohesiveness of the groups as a whole.

Aside from THA, Theia 92 has the most objects with X-ray luminosities. Comparing those two groups, we find that Theia 92 has a comparable density to THA between Gaia $(G - G_{RP}) = 0.45$–0.6, but the Theia 92 objects trend toward a higher X-ray luminosity. Increased X-ray luminosity is interpreted as increased chromospheric activity and younger stars (Malo et al. 2014). The majority of these objects are outside the *UVW* cuts described in Section 2.4, and are not kinematically similar to the core of IC 2602. It is challenging to attribute this to an age difference though, as all the objects overlap in range with Pleiades stars.

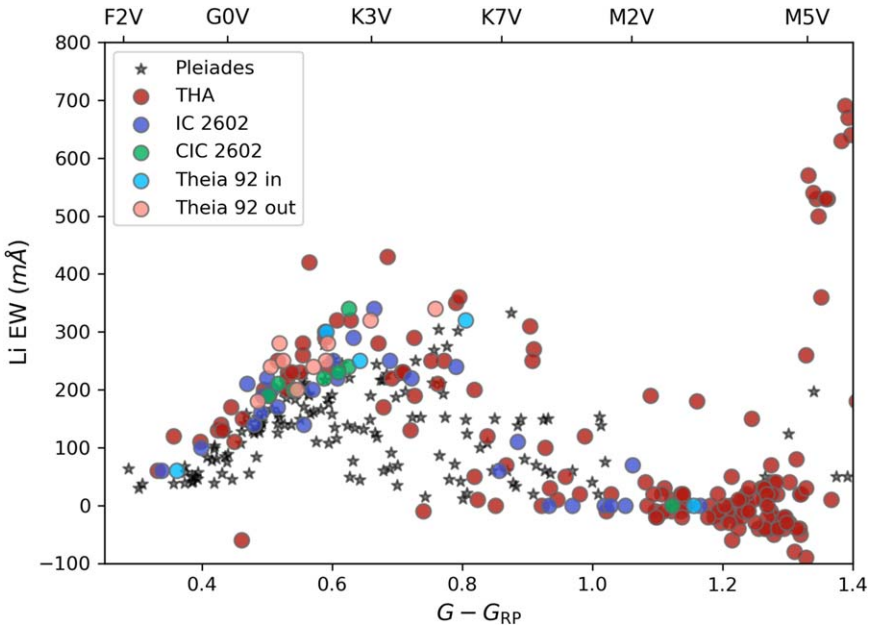

Figure 13. EW values for the Li I 6708 Å line for objects in our membership list plotted across Gaia ($G - G_{RP}$). Pleiades values from Bouvier et al. (2018) are in the background as black stars, and equivalent spectral types run across the top axis. Without full color coverage for every group we cannot use Li dating techniques, but in general are consistent with THA distributions, and above those of Pleiades with some overlap.

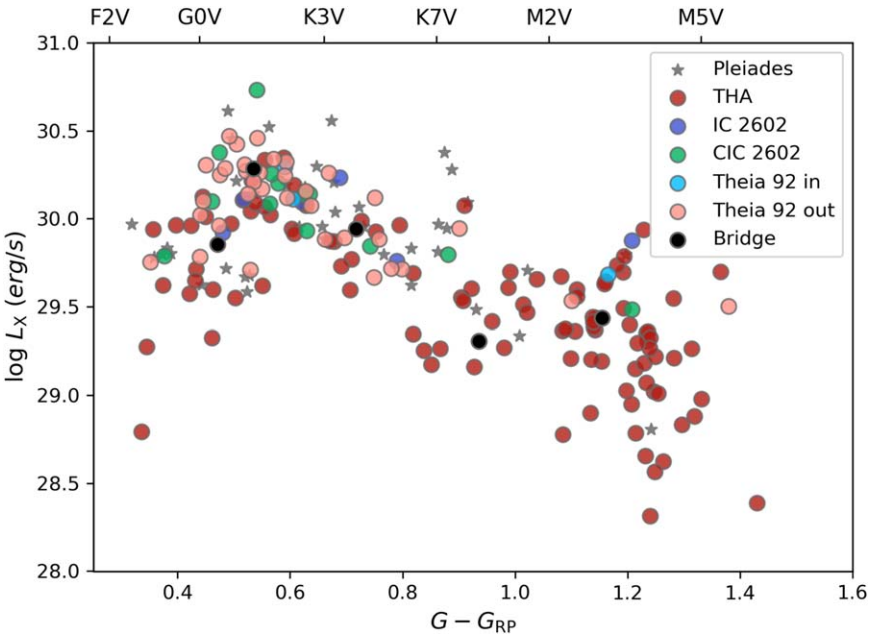

Figure 14. The X-ray luminosity of our sample where X-ray flux values are available, plotted across Gaia ($G - G_{RP}$). Pleiades values are in the background as black stars, and equivalent spectral types run across the top axis.

6. Light-curve Amplitudes for FGK stars

Morris (2020) compiled the rotation periods and photometric amplitudes of FGK stars in six clusters and associations of different ages and found that the median amplitude of the groups decreased with age.

We put the amplitudes we measured in this work into context with the amplitude–age relation presented in Morris (2020). We note that our calculation of amplitude varies slightly from the "smoothed amplitude" used in Morris (2020) and defined in Douglas et al. (2017). Those works use the phase-folded light curve and calculated the difference between the maximum and minimum after it has been smoothed by a Gaussian kernel, whose width in cadences was determined depending on the source of the light curve (i.e., TESS, Kepler, or K2). Instead, we simply calculate the difference between the 5th and 95th percentile of flux in the light curve as the amplitude. In Figure 15 we show how these methods compare for one of our objects previously shown in Figure 3. We found that the values were within 10%, and considered them comparable.

In Figure 16 we add the ∼40 Myr stars to the analysis of smoothed amplitude versus age from Morris (2020). We use only the objects with confirmed rotation periods from this work (those with a Flag value of 0 in Table 2) and those from

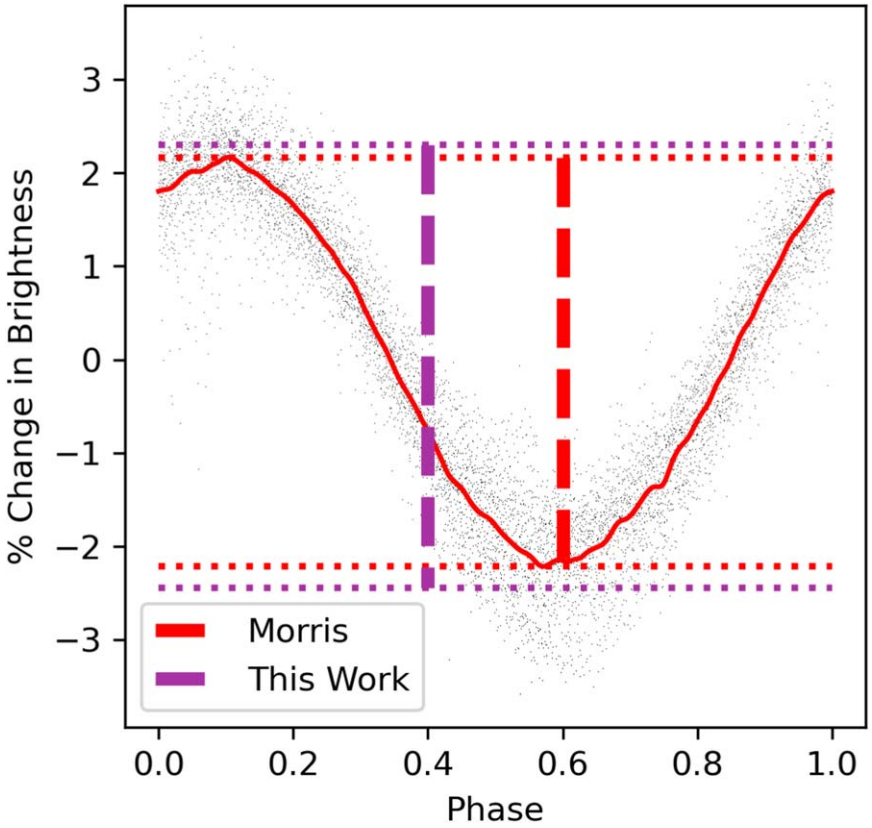

Figure 15. The TESS phase-folded light curve of Gaia DR3 5239868587976272896. In red is the data smoothed by a Gaussian kernel every 50 cadences, the method used to measure the smoothed amplitude for TESS light curves in Morris (2020). Red horizontal lines extend from the top and bottom of the smoothed curve, and a red vertical line details the amplitude. In horizontal purple lines extend from the 5th and 95th percentile value for the flux, and the purple vertical line represents that amplitude. The difference is less than 10%.

Popinchalk et al. (2023), and made a cut on Gaia $(G - G_{RP}) \leqslant 1.0$ in an attempt to limit our sample to just FGK stars. We then had 48, 37, 53, and 5 objects from IC 2602, THA, CIC 2602, and the bridge group, respectively. We grouped all of our objects into a representative 40 Myr association.

In the left part of Figure 16, the six groups used in Morris (2020) are shown color coded by age. They represent Upper Scorpius (10 Myr), Upper Centaurus Lupus (16 Myr), Pisces–Eridanus (120 Myr; Curtis et al. 2019), Praesepe (650 Myr; Douglas et al. 2017), NGC 6811 (1 Gyr; Curtis et al. 2019), and M67 (4 Gyr; Gonzalez 2016). Our 40 Myr sample shares the same qualitative color coding.[10]

Morris (2020) calculated a best-fit line through the median smoothed amplitudes of the associations, which we recreate in gray dashes. The amplitudes from our ∼40 Myr representative group are consistent and sit on the best-fit line.

In the right part of Figure 16 we look at the same groups that are 40 Myr or older and investigate their amplitudes across Gaia $(G - G_{RP})$ color. We exclude the younger groups (Upper Scorpius and UCL) as they had relatively small sample sizes (19 and 34 objects, respectively). For the five other groups we calculate the median and 16th and 84th percentiles for five evenly spaced color bins from 0.32 to 1.0, meant to represent a range of spectral types from F5 to M0. We see that generally for each color bin the amplitude decreases with age. However, there appears to be a color dependence on amplitude at a given age as well as the trend within each bin.

[10] amplitudes and periods come from Morris (2020) unless otherwise noted, see Morris (2020) for full details.

7. Discussion

7.1. Gyrochronology of IC 2602, CIC 2602, and Theia 92

In this section, we move beyond the straightforward description of the rotation periods presented in Section 4 and add our interpretation of them to attempt to constrain the age of the groups presented.

The distribution of rotation rates across spectral types for IC 2602 is consistent with THA, CIC 2602, and the small bridge group between THA and IC 2602. As noted in Section 4, this similarity in shape on the color–period diagram for groups with ∼40 Myr ages strongly implies a shared age. Gyrochronology often focuses on the slow-rotator sequence, but the similarity between the three associations implies that there is still some typical rotation period distribution, even if it is not a well-defined slow-rotator sequence until ∼100 Myr.

Furthermore, in Figure 17 we present the rotation periods of FGK stars in IC 2602, CIC 2602, the bridge group, and THA compared to those of the Pleiades (Rebull et al. 2016). We do this as the Pleiades are a well-studied benchmark cluster that is slightly older (∼120 Myr) and therefore slightly more evolved than any of the groups we analyzed herein. The Pleiades have a well-defined slow-rotator sequence through to the K regime, as shown by the small spread in scatter of rotation period at a given color, typically only ∼2 days.

Popinchalk et al. (2021) suggest that the color at which the slow-rotator sequence is converged to in the M dwarf regime could be a tool for understanding the age of hundreds of Myr populations of stars. If we extend that idea into the FGK

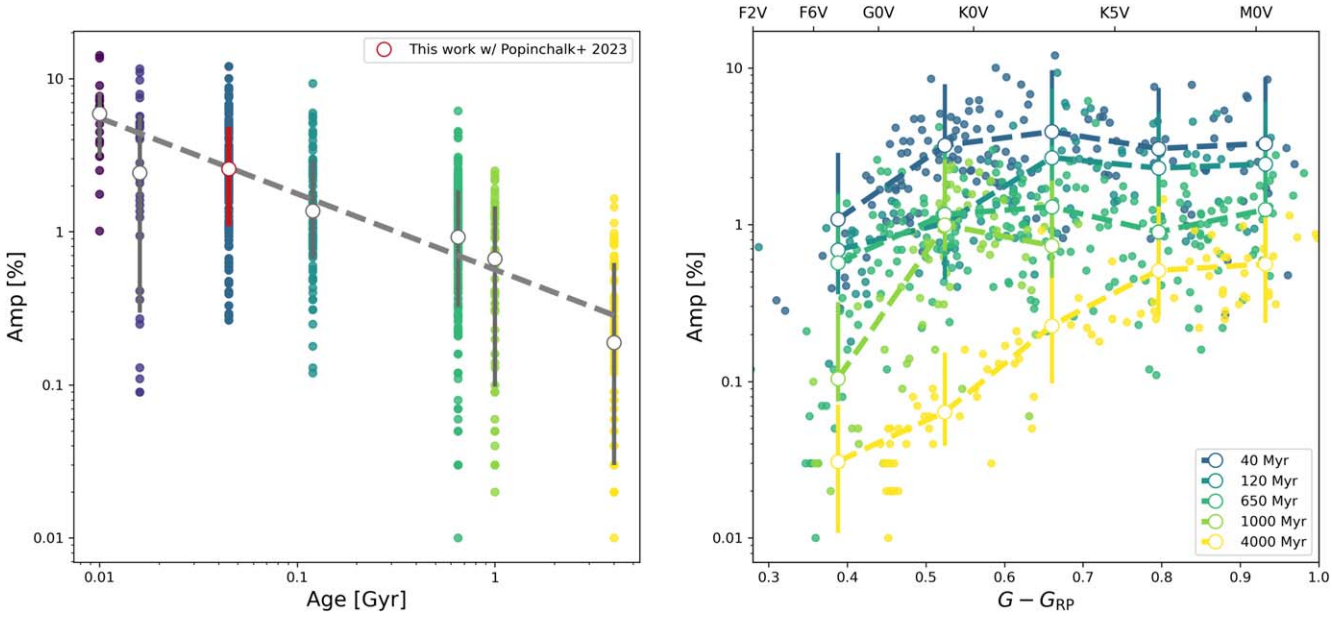

Figure 16. Left: the amplitude of variability for our ∼40 Myr FGK stars on top of a recreation of Figure 3 from Morris (2020). Groups used in Morris (2020) are presented and include from youngest to oldest: Upper Scorpius, Upper Centaurus Lupus, Pisces–Eridanus, Praesepe, NGC 6811, and M67. Points are color coded by age and their median amplitude with 16th and 84th percentile error bars are in gray. We combine the amplitudes we measured from the FGK stars of IC 2602, CIC 2602, and the bridge group as well as those in THA from Popinchalk et al. (2023) at 40 Myr of age in the same color map, with the median and percentiles in red. The best fit for the amplitude–age relation from Morris (2020) is the gray dashed line, and our new amplitudes agree well. Right: the 40 Myr and older groups from the left panel shown with amplitude vs. Gaia ($G - G_{RP}$). The younger groups were excluded due to their small sample size. The dotted line shows the medians and 16th and 84th percentiles for five evenly spaced color bins between Gaia ($G - G_{RP}$) = 0.32–1.0 for each group. We see that the general trend of larger amplitude at younger ages is consistent across color, but the relation appears to be color dependent.

regime, we can look at Figure 17 with these populations of 40 Myr stars and see that they overlap well with the Pleiades rotation period distribution up to Gaia ($G - G_{RP}$) = 0.5. We speculate that the wide spread of G-type stars mentioned in Section 4.1 might be caused by stars at different states of convergence to the slow-rotator sequence.

With regards to Theia 92, across the population there is a wide range of periods. If the group is considered cohesive, then the distribution measured could imply an extended period of star formation over tens of millions of years. This could be why there is no clear gyrochronology sequence developing. Alternatively, the inherent scatter of rotation periods in populations ∼10 Myr (e.g., Rebull et al. 2018; Douglas et al. 2024) does mean that it could have a single age.

After the UVW cuts described in Section 2.4 were applied to try and distinguish the most kinematically coherent component of the IC 2602 core group, there was still less agreement with all other associations. Considering the two UVW cuts we made separately, the "in" group suffers from small numbers in the FGK regime, which makes any sequence difficult to discern. However, all the rotation periods for this subgroup in Figure 11 are $<$ 10 days. This implies that the stars are young ($<$ 100 Myr), even if their association with a certain age is difficult to define. Furthermore, the "out" group that is linked with Platais 8 shows signs of being a similar age to IC 2602 given its relative dearth of rapid rotators in the FGK regime. All the rotation periods in the FGK regime are at ∼10 days or less which implies they are all young, at most Pleiades age (∼120 Myr), but likely younger. Gagné et al. (2021) note that Platais 8 is poorly characterized, with an estimated age of ∼60 Myr (Platais et al. 1998). This is not too significant an age difference, as Douglas et al. (2024) found that groups aged 25–55 Myr had similar rotation period distributions. As suggested in Gagné et al. (2021), further investigation of the Platais 8 group would go far in understanding how it has, or may still be, interacting with the IC 2602 moving group, including this subset of Theia 92.

Finally, the agreement of the M dwarf stars in all the groups should not be interpreted as strong evidence for a shared age. M dwarfs evolve differently than other main-sequence stars, especially in terms of their angular momentum (e.g., Matt et al. 2015; Popinchalk et al. 2021; Kounkel et al. 2022). As shown in Figure 8 of Popinchalk et al. (2023), the THA distribution of early- to mid-M dwarfs sits directly on top of the Pleiades (Rebull et al. 2016). Kounkel et al. (2022) found a similar overlap for a larger group of stars, and were able to disentangle ages by considering the angular momentum of the stars using mass and radii estimates. They imply that after some initial contraction as the stars enter the ZAMS in the first approximately tens of Myr, they will overlap in rotation period space as the spin up due to contraction is mediated by magnetic braking, even while the overall angular momentum increases. So, while there is good agreement from all the groups in this work along the M dwarf rotation period sequence, it simply implies a young population and is not strong evidence for a cohesive age group nor is it strong evidence for a coeval age.

7.2. Other Age Diagnostics

The main takeaway from the Li EW and X-ray luminosity distributions of the objects analyzed herein and shown in Figures 13 and 14 is that they are consistent with being young. It is challenging to draw specific conclusions or comparisons of age due to the inherent scatter at this age. We do note that in Figures 13 and 14, Theia 92 objects sit above those of the well-sampled THA population, which could hint at a younger age for Theia 92. However, there are currently

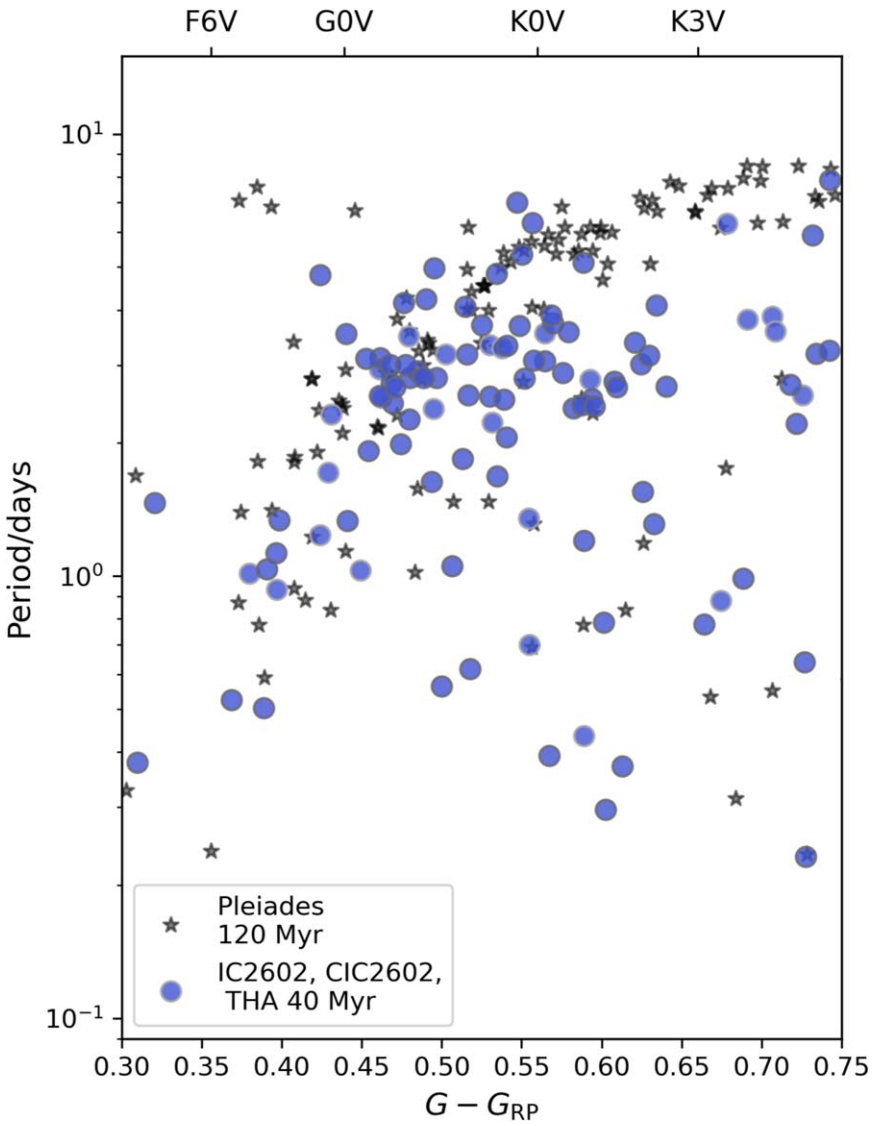

Figure 17. Same as Figure 10, but the rotation periods of IC 2602, CIC 2602, and THA combined (blue) and compared with small black stars representing the rotation period distribution of the Pleiades from Rebull et al. (2016). The color axis is focused on the range of FGK stars. Notice the general agreement with the Pleiades slow-rotator sequence from F toward G0, before the IC 2602, THA, and CIC 2602 begin to diverge.

not enough measurements across the full range of spectral types to be able to say anything definitively. Dividing the objects into the kinematic subsets from Section 2.4 would make it worse. It is conclusive that the stars of Theia 92 are largely young, but inconclusive if they form a cohesive, coeval structure.

In regards to the general agreement of the amplitude across age trend shown in Figure 15 described in Morris (2020), we find it encouraging that the FGK stars in these ∼40 Myr groups fit almost precisely into the trend. Furthermore, we show that this trend is consistent across Gaia ($G - G_{RP}$) color (and therefore spectral type), and seems to vary with color. It is worth noting that five of the six groups analyzed by Morris (2020) are open clusters, with only Pisces–Eridanus being a "stellar stream" like those in our sample. TESS is exceptionally positioned to add significant numbers of rotation periods (and therefore amplitudes) for young moving groups. Hence, with the all-sky capability of TESS and the numerous large-area stellar streams and moving groups uncovered in Gaia, the amplitude relation can soon be populated with many more groups to potentially calibrate another lever arm for age-dating diagnostics.

7.3. Interesting Light Curves

We remain agnostic to the cause of the multiple period, beat pattern, and eclipsing binary light curves discussed in Section 3.3.1, as ultimately RV monitoring is required to confirm a binary system. However, follow-up programs will do well to combine the light-curve analysis with Gaia DR3 RUWE to go after the most promising candidates. For example, selecting objects with both an anomalous RUWE value and a light curve with evidence of binarity (represented as purple circles with a blue, orange, or green point in Figure 6).

8. Conclusion

Creating a sample from membership lists of IC 2602, CIC 2602, Theia 92, and a bridge group we identify 953 objects that could be part of a larger group along with THA. From that sample we measure 636 rotation periods, and present the first

rotation period distributions of IC 2602, CIC 2602, Theia 92, and the bridge group in Section 4.

We identify several potential binary candidates from Gaia DR3 RUWE values as well as eclipsing binaries and beat binaries from a light-curve analysis. Furthermore, we identify four new complex rotators which all show morphological change across three cycles of TESS, with later cycles and shorter cadences revealing details not immediately apparent from Cycle 1.

We present for the first time a bridge group of stars that serve as a physical connection between IC 2602 and THA, which is kinematically and age coherent. We find that the rotation periods of IC 2602, CIC 2602, the THA to IC 2602 bridge and THA overlap convincingly in the shape of their gyrochronology, implying a very similar age. This encourages the further exploration of other young moving groups with similar XYZUVW properties such as Carina and Columba. The rotation period distribution of Theia 92 appears scattered even after selecting only part of the sample with similar *UVW* kinematics. We conclude that Theia 92 is likely a mix of ages, all young.

We explore lithium EW measurement where available as well as X-ray luminosities, and find the representative members of each group analyzed implied similarity in age inclusive of Theia 92. This was further evidence of the cohesiveness of the groups composing a structure that is currently dissolving. When we consider the amplitudes of the variability of the whole data set, they fall precisely on the amplitude–age relationship in Morris (2020) at ∼40 Myr, and we show that the amplitude–age relationship appears to include a color dependence.

Acknowledgments

This work is supported by NASA TESS GI grant No. 80NSSC21K0792 and No. 80NSSC19K1708. This work was supported in part by the National Science Foundation under grant No. NSF PHY-1748958. J.L.C. is supported by NSF AST-2009840 and NASA TESS GI grant No. 80NSSC22K0299 (G04217). J.F. acknowledges the continuous support of the Heising Simons Foundation for this work.

Much of this work was done by participants in the AMNH Masters in Teaching program and Science Research and Mentoring Program. The author list reflects the contributions of those involved, but M.P. and J.F. also thank the organizers of those programs for their participation.

Facilities: TESS, Gaia.

Software: `Astropy` (Astropy Collaboration et al. 2013; The Astropy Collaboration et al. 2018), `astroquery` (Ginsburg et al. 2019), `Matplotlib` (Hunter 2007), `NumPy` (Harris et al. 2020), `pandas` (McKinney 2010), `Photutils` (Bradley et al. 2016), `TESScut` (Brasseur et al. 2019), `tess_cpm` (beta version from 2019; the published version is now called `unpopular`; Hattori et al. 2022).

ORCID iDs

Mark Popinchalk https://orcid.org/0000-0001-9482-7794
Jacqueline K. Faherty https://orcid.org/0000-0001-6251-0573
Jonathan Gagné https://orcid.org/0000-0002-2592-9612
Jason L. Curtis https://orcid.org/0000-0002-2792-134X
Leslie Moranta https://orcid.org/0000-0001-7171-5538
Rocio Kiman https://orcid.org/0000-0003-2102-3159
Dominic Couture https://orcid.org/0000-0003-2604-3255

References

Agüeros, M. A., Bowsher, E. C., Bochanski, J. J., et al. 2018, ApJ, 862, 33
Andrews, J. J., Chanamé, J., & Agüeros, M. A. 2017, MNRAS, 472, 675
Angus, R., Price-Whelan, A. M., Zinn, J. C., et al. 2022, AJ, 164, 25
Astropy Collaboration, Robitaille, T. P., Tollerud, E. J., et al. 2013, A&A, 558, A33
Barlow, B. N., Corcoran, K. A., Parker, I. M., et al. 2022, ApJ, 928, 20
Barnes, S. A. 2003, ApJ, 586, 464
Barnes, S. A., Sofia, S., Prosser, C. F., & Stauffer, J. R. 1999, ApJ, 516, 263
Barnes, S. A., Weingrill, J., Fritzewski, D., Strassmeier, K. G., & Platais, I. 2016, ApJ, 823, 16
Basri, G., & Nguyen, H. T. 2018, ApJ, 863, 190
Belokurov, V., Penoyre, Z., Oh, S., et al. 2020, MNRAS, 496, 1922
Boller, T., Freyberg, M. J., Trümper, J., et al. 2016, A&A, 588, A103
Bouvier, J., Barrado, D., Moraux, E., et al. 2018, A&A, 613, A63
Boyle, A. W., & Bouma, L. G. 2023, AJ, 166, 14
Bradley, L., Sipocz, B., Robitaille, T., et al. 2016, Photutils: Photometry tools, Astrophysics Source Code Library, ascl:1609.011
Brasseur, C. E., Phillip, C., Fleming, S. W., Mullally, S. E., & White, R. L. 2019, Astrocut: Tools for creating cutouts of TESS images, Astrophysics Source Code Library, ascl:1905.007
Cao, L., & Pinsonneault, M. H. 2022, MNRAS, 517, 2165
Curtis, J. L., Agüeros, M. A., Douglas, S. T., & Meibom, S. 2019, ApJ, 879, 49
Curtis, J. L., Agüeros, M. A., Mamajek, E. E., Wright, J. T., & Cummings, J. D. 2019, AJ, 158, 77
Curtis, J. L., Agüeros, M. A., Matt, S. P., et al. 2020, ApJ, 904, 140
da Silva, L., Torres, C. A. O., de La Reza, R., et al. 2009, A&A, 508, 833
D'Antona, F., & Mazzitelli, I. 1994, ApJS, 90, 467
de Zeeuw, P. T., Hoogerwerf, R., de Bruijne, J. H. J., Brown, A. G. A., & Blaauw, A. 1999, AJ, 117, 354
Deacon, N. R., & Kraus, A. L. 2020, MNRAS, 496, 5176
Dobbie, P. D., Lodieu, N., & Sharp, R. G. 2010, MNRAS, 409, 1002
Douglas, S. T., Agüeros, M. A., Covey, K. R., & Kraus, A. 2017, ApJ, 842, 83
Douglas, S. T., Cargile, P. A., Matt, S. P., et al. 2024, ApJ, 962, 16
Douglas, S. T., Curtis, J. L., Agüeros, M. A., et al. 2019, ApJ, 879, 100
Dungee, R., van Saders, J., Gaidos, E., et al. 2022, ApJ, 938, 118
Eggen, O. J., Freeman, K. C., & Rodgers, A. W. 1973, RPPh, 36, 625
Gagné, J., David, T. J., Mamajek, E. E., et al. 2020, ApJ, 903, 96
Gagné, J., Faherty, J. K., Moranta, L., & Popinchalk, M. 2021, ApJL, 915, L29
Gagné, J., Mamajek, E. E., Malo, L., et al. 2018a, ApJ, 856, 23
Gaia Collaboration, Prusti, T., de Bruijne, J. H. J., et al. 2016, A&A, 595, A1
Gaia Collaboration, Vallenari, A., Brown, A. G. A., et al. 2023, A&A, 674, A1
Gieseking, F. 1981, A&AS, 43, 33
Ginsburg, A., Sipőcz, B. M., Brasseur, C. E., et al. 2019, AJ, 157, 98
Gonzalez, G. 2016, MNRAS, 463, 3513
Gruner, D., Barnes, S. A., & Weingrill, J. 2023, A&A, 672, A159
Günther, M. N., Berardo, D. A., Ducrot, E., et al. 2022, AJ, 163, 144
Harris, C. R., Millman, K. J., van der Walt, S. J., et al. 2020, Natur, 585, 357
Hattori, S., Foreman-Mackey, D., Hogg, D. W., et al. 2022, AJ, 163, 284
Hoogerwerf, R., & Aguilar, L. A. 1999, MNRAS, 306, 394
Hunter, J. D. 2007, CSE, 9, 90
Kiman, R., Faherty, J. K., Cruz, K. L., et al. 2021, AJ, 161, 277
Koen, C. 2023, MNRAS, 518, 2921
Kołaczek-Szymański, P. A., Pigulski, A., Michalska, G., Moździerski, D., & Różański, T. 2021, A&A, 647, A12
Kounkel, M., & Covey, K. 2019, AJ, 158, 122
Kounkel, M., Stassun, K. G., Bouma, L. G., et al. 2022, AJ, 164, 137
Kraus, A. L., Shkolnik, E. L., Allers, K. N., & Liu, M. C. 2014, AJ, 147, 146
Lindegren, L., Klioner, S. A., Hernández, J., et al. 2021, A&A, 649, A2
Lindegren, L., Lammers, U., Hobbs, D., et al. 2012, A&A, 538, A78
Lomb, N. R. 1976, Ap&SS, 39, 447
Luhman, K. L. 2022, AJ, 164, 151
Luhman, K. L. 2023, AJ, 165, 269
Malo, L., Artigau, É., Doyon, R., et al. 2014, ApJ, 788, 81
Mamajek, E. E., & Hillenbrand, L. A. 2008, ApJ, 687, 1264
Markarian, B. E. 1953, CoBAO, 11, 19
Matt, S. P., Brun, A. S., Baraffe, I., Bouvier, J., & Chabrier, G. 2015, ApJL, 799, L23
McKinney, W. 2010, in Proc. of the 9th Python in Science Conf., ed. S. van der Walt & J. Millman, 61
Meibom, S., Barnes, S. A., Latham, D. W., et al. 2011, ApJL, 733, L9
Meibom, S., Barnes, S. A., Platais, I., et al. 2015, Natur, 517, 589
Meingast, S., Alves, J., & Fürnkranz, V. 2019, A&A, 622, L13
Meingast, S., Alves, J., & Rottensteiner, A. 2021, A&A, 645, A84
Mejías, A., Minniti, D., Alonso-García, J., et al. 2022, A&A, 660, A131
Morris, B. M. 2020, ApJ, 893, 67

Nisak, A. H., White, R. J., Yep, A., et al. 2022, AJ, 163, 278
Núñez, A., Agüeros, M. A., Covey, K. R., et al. 2022, ApJ, 931, 45
Palumbo, E. K., Montet, B. T., Feinstein, A. D., et al. 2022, ApJ, 925, 75
Paudel, R. R., Gizis, J. E., Burgasser, A. J., & Hsu, C. 2019, MNRAS, 486, 4144
Pecaut, M. J., & Mamajek, E. E. 2013, ApJS, 208, 9
Platais, I., Kozhurina-Platais, V., & van Leeuwen, F. 1998, AJ, 116, 2423
Popinchalk, M., Faherty, J. K., Curtis, J. L., et al. 2023, ApJ, 945, 114
Popinchalk, M., Faherty, J. K., Kiman, R., et al. 2021, ApJ, 916, 77
Rampalli, R., Agüeros, M. A., Curtis, J. L., et al. 2021, ApJ, 921, 167
Randich, S., Aharpour, N., Pallavicini, R., Prosser, C. F., & Stauffer, J. R. 1997, A&A, 323, 86
Randich, S., Pallavicini, R., Meola, G., Stauffer, J. R., & Balachandran, S. C. 2001a, A&A, 372, 862
Randich, S., Pallavicini, R., Meola, G., Stauffer, J. R., & Balachandran, S. C. 2001b, A&A, 372, 862
Rebull, L. M., Stauffer, J. R., Bouvier, J., et al. 2016, AJ, 152, 113
Rebull, L. M., Stauffer, J. R., Cody, A. M., et al. 2018, AJ, 155, 196
Reinhold, T., Reiners, A., & Basri, G. 2013, A&A, 560, A4
Ricker, G. R., Winn, J. N., Vanderspek, R., et al. 2015, JATIS, 1, 014003
Röser, S., Schilbach, E., & Goldman, B. 2019, A&A, 621, L2
Scargle, J. D. 1982, ApJ, 263, 835
Shan, Y., Yee, J. C., Bowler, B. P., et al. 2017, ApJ, 846, 93
Shkolnik, E. L., & Barman, T. S. 2014, AJ, 148, 64
Skumanich, A. 1972, ApJ, 171, 565
Stassun, K. G., & Torres, G. 2021, ApJL, 907, L33
Stauffer, J., Collier Cameron, A., Jardine, M., et al. 2017, AJ, 153, 152
Stauffer, J., Rebull, L., David, T. J., et al. 2018b, AJ, 155, 63
Stauffer, J., Rebull, L. M., Cody, A. M., et al. 2018a, AJ, 156, 275
Stauffer, J. R., Schultz, G., & Kirkpatrick, J. D. 1998, ApJL, 499, L199
The Astropy Collaboration, Price-Whelan, A. M., Sipőcz, B. M., et al. 2018, AJ, 156, 123
Tokovinin, A., & Briceño, C. 2018, AJ, 156, 138
Torres, C. A. O., da Silva, L., Quast, G. R., de la Reza, R., & Jilinski, E. 2000, AJ, 120, 1410
Torres, C. A. O., Quast, G. R., da Silva, L., et al. 2006, A&A, 460, 695
van Leeuwen, F. 1999, A&A, 341, L71
West, A. A., Weisenburger, K. L., Irwin, J., et al. 2015, ApJ, 812, 3
Wood, M. L., Mann, A. W., Barber, M. G., et al. 2023, AJ, 165, 85
Zhan, Z., Günther, M. N., Rappaport, S., et al. 2019, ApJ, 876, 127
Zuckerman, B., & Song, I. 2004, ARA&A, 42, 685
Zuckerman, B., Song, I., & Webb, R. A. 2001, ApJ, 559, 388
Zuckerman, B., & Webb, R. A. 2000, ApJ, 535, 959